

**Authors' response to comments on "Instrument Artifacts Lead to Uncertainties in Parameterizations of Cloud Condensation Nucleation", Revised Submission, Referee #1**

**Authors' response:** We thank the Reviewer for her/his detailed feedback. In particular, we agree with the Reviewer that our assumptions regarding volume weighted components of kappa warranted revision and we have now revised that section accordingly. Specific modifications are discussed below.

**General Comments**

- 1) **Reviewer comment:** The authors responded to my comment. For Part B, I suggest that this response regarding to what extent the artifacts investigated here can explain the discrepancies in the kappa in the literature should be also incorporated into the revised manuscript.

**Authors' response:** Agree. This was an oversight on our part. We have now added this discussion to the manuscript.

**Authors' changes to the manuscript:** Page 18 Lines 320-325 the text now reads: "This analysis was also applied to the range of apparent hygroscopicity values Svenningsson et al., 2006 found for ammonium nitrate  $0.577 \leq \kappa_{app} \leq 0.753$ , with a mean value of 0.670. If 0.670 is assumed to be the true  $\kappa_{app}$  for ammonium nitrate, then the sample/sheath ratio used to determine  $\kappa_{app}$  ( $1.2-2 \text{ L min}^{-1}$ ) could lead an experimental kappa as low as 0.665 or as high as 0.674, which would not fully explain the actual experimental range. This assessment ignores possibility of under/over counting which could introduce additional errors."

- 2) **Reviewer comment:** Regarding my formed general comment 2

A. I think that the assumption of the "volume-weighted approach accepted as a standard convention of kappa theory" is that different components are internally mixed on particles! Particles at different sizes are apparently not internally mixed. Taking an extreme example, if an aerosol population consists of black carbon particles for all particles <100 nm and (NH<sub>4</sub>)<sub>2</sub>SO<sub>4</sub> particles for all particle >100 nm. If one measure D50 at 0.1% one would get a D50 of ~140 nm since the D50 of (NH<sub>4</sub>)<sub>2</sub>SO<sub>4</sub> is ~140 nm. And from that D50 vs. SS, one would get a kappa of ~0.6 (the kappa value of (NH<sub>4</sub>)<sub>2</sub>SO<sub>4</sub>). Of course, the D50 vs. SS data sets obtained in this Case will not fall on the lines of constant kappa.

B. This again leads to my concern about the approach used to derive artifacts from DMA in this study because it is different from the real CCN measurement. To clarify my comment, in the real CCN measurement, at first activated fractions of particles are

obtained, either activated fraction vs. supersaturation(SS) for particles of a given size or activated fraction vs. particle size at a given SS. The activation curve is then fitted to derive a D50 or SS50 and from D50 vs. SS or D vs. SS50, kappa is obtained. In order to investigate the uncertainties of kappa due to instrument artifacts, one would need simulate the data acquisition process of CCN activation measurement by simulating the number of particles and number of activated particles in each size bin (in the Case of D50 vs. SS) and then activation fraction and D50. I am not sure whether the artifacts in this study can reflect the real uncertainties in CCN measurement and is useful to get an idea of the uncertainties in CCN measurement.

**A. Authors' response:** The reviewer is correct, and we thank the reviewer for identifying this flaw in our previous analysis. Specifically, equation 12, read

$$\kappa_{app,theory} = \sum_i \epsilon_i \kappa_i \quad (12)$$

where  $\epsilon_i$  is the volume fraction of aerosol of each diameter  $i$ , and  $\kappa_i$  is the perceived  $\kappa_{app}$  for each diameter (adapted from Petters and Kreidenweis [2007]). In this equation, there is an underlying assumption that all particles of a certain size have a certain composition, and that variations in composition (and thus kappa) occur only with corresponding variations in size. Since this assumption doesn't hold true for all aerosol populations, we have revised the analysis to include the active fraction as described below.

**B. Authors' response:** The conceptual changes detailed in 2A have been applied to the assessment of apparent hygroscopicity artifacts derived from DMA measurements.

**Authors' changes to the manuscript to address the issues raised in 2A&B:** In addition to the text below, Figures 4 and 10 have been updated, and Supplemental Figure S2 has been added.

Pages 16-17 Lines 272-317 the text now reads: "To test how uncertainties in DMA diameter translate to uncertainties in  $\kappa_{app}$ , the activation of particles downstream of the DMA was assessed. First, for each case and diameter (25, 50, 100, and 200 nm) the critical saturation ratio  $S_{crit}$  was calculated for each particle diameter range downstream from the DMA using Eq. 3a. These critical saturation ratios were converted to critical percent supersaturation  $SS_{crit}$  and used to calculate the activated fraction  $AF$  for the aerosol particles downstream from the DMA for percent supersaturations  $0.01 < SS < 1.5$ , using the equation:

$$AF = \frac{1}{2} \left( 1 + \operatorname{erf} \left( \frac{SS - SS_{crit}}{\sigma \sqrt{2}} \right) \right) \quad (12)$$

Where the standard deviation  $\sigma$  was equal to one-hundredth of  $SS_{crit}$ . The small  $\sigma/SS_{crit}$  ratio was chosen in order to generate accurate activated fraction curves for each particle diameter.

The activated fraction curve for each selected diameter (25, 50, 100, and 200 nm) was then calculated as the sum of the number-weighted activated fractions of each particle diameter downstream from the DMA. For example, for a selected diameter of 25 nm, the downstream diameters ranged from 23 nm to 27 nm for DMA Case 1 and from 20 nm to 36 nm in DMA Case 4. The equation used for this calculation is:

$$AF_{weighted} = \sum_i \frac{n_i}{n_{total}} AF_i \quad (13)$$

where  $AF_i$  is the activated fraction calculated using Eq. 12 and  $\frac{n_i}{n_{total}}$  is the fraction of particle downstream from the DMA of diameter  $i$ .

This calculation was repeated for each selected diameter (25, 50, 100, and 200 nm), each DMA Case (1-7), and percent supersaturation (0.01-1.5) in order to construct activation curves for each selected diameter and DMA Case. As an example, in Fig. S2, the shape and position of each activated fraction curve vary with the DMA flow ratios. As the aerosol/sheath ratio increases, the activated fraction curve flattens out (DMA Case 4). The critical percent supersaturation  $SS_{crit}$  was then determined for each activation curve as the percent supersaturation where  $AF = 0.50$ . These results are shown in Fig. 4a for ammonium sulfate and sodium chloride. Eq. 4 was then used to calculate  $\kappa_{app,theory}$  for each DMA Case and selected diameter, as shown in Fig. 4b. Discrepancies between  $\kappa_{app,theory}$  calculated in this study and literature values (hereon referred to as “ $\kappa_{app}$  artifacts”) are shown for both compounds in Fig. 4c-d.

The largest  $\kappa_{app}$  artifact was found in DMA case 4 (where the aerosol/sheath ratio was the highest) for both ammonium sulfate and sodium chloride aerosols. The artifacts for 25 nm ammonium sulfate aerosol in DMA case 4 was 0.08, or ~13% of the literature value used for  $\kappa_{app}^{(NH_4)_2SO_4}$ , while the artifacts for 25 nm sodium chloride in DMA case 4 was 0.16, or ~13% of the literature value used for  $\kappa_{app}^{NaCl}$ . Artifacts were also high for DMA case 6 ( $-0.041 \leq \kappa_{app,artifact}^{(NH_4)_2SO_4} \leq -0.048$ ) and DMA case 7 ( $0.014 \leq \kappa_{app,artifact}^{(NH_4)_2SO_4} \leq 0.024$ ), where sheath and excess flow were unequal. This result demonstrates that artifacts may still occur when low aerosol/sheath flow ratios are chosen (0.15 and 0.08 for DMA cases 6 and 7, respectively) due to small differences between sheath and excess flow rates (5% and 2% for DMA cases 6 and 7, respectively).

$\kappa_{app}$  artifacts were larger for sodium chloride ( $-0.10 \leq \kappa_{app,artifact}^{NaCl} \leq 0.16$ ) than for ammonium sulfate ( $-0.05 \leq \kappa_{app,artifact}^{(NH_4)_2SO_4} \leq 0.08$ ) across the DMA cases. As our results show, when two or more compounds are compared, the more hygroscopic compound will have larger  $\kappa_{app}$  artifacts.”

The edited Fig. 4 is shown below.

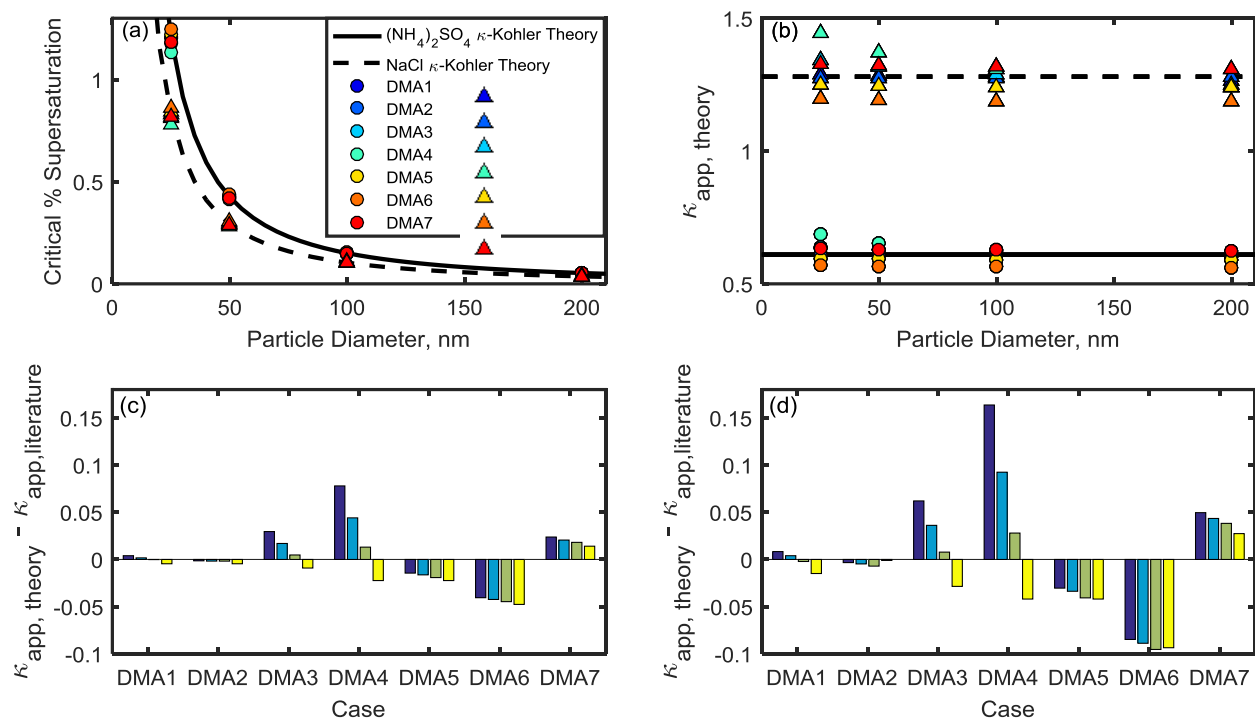


**Figure 4** (a) Critical supersaturation of ammonium sulfate and sodium chloride particles calculated for DMA Cases 1-7 for sodium chloride (triangles) and ammonium sulfate (circles). Ammonium sulfate and sodium chloride curves from  $\kappa$ -Köhler theory are shown for comparison. (b) Apparent hygroscopicity  $\kappa_{app}$  for DMA Cases 1-7. (c) DMA-flow-derived artifacts in ammonium sulfate  $\kappa_{app}$  are shown for each DMA case. (d) DMA-flow-derived artifacts in sodium chloride  $\kappa_{app}$  are shown for each DMA case.

Fig. 10 has also been edited in order to include these new results.

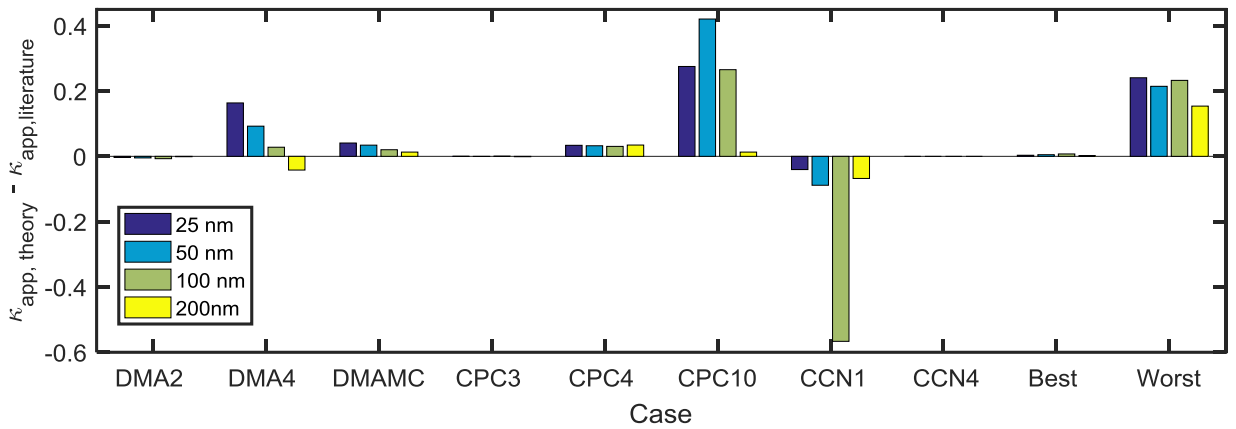
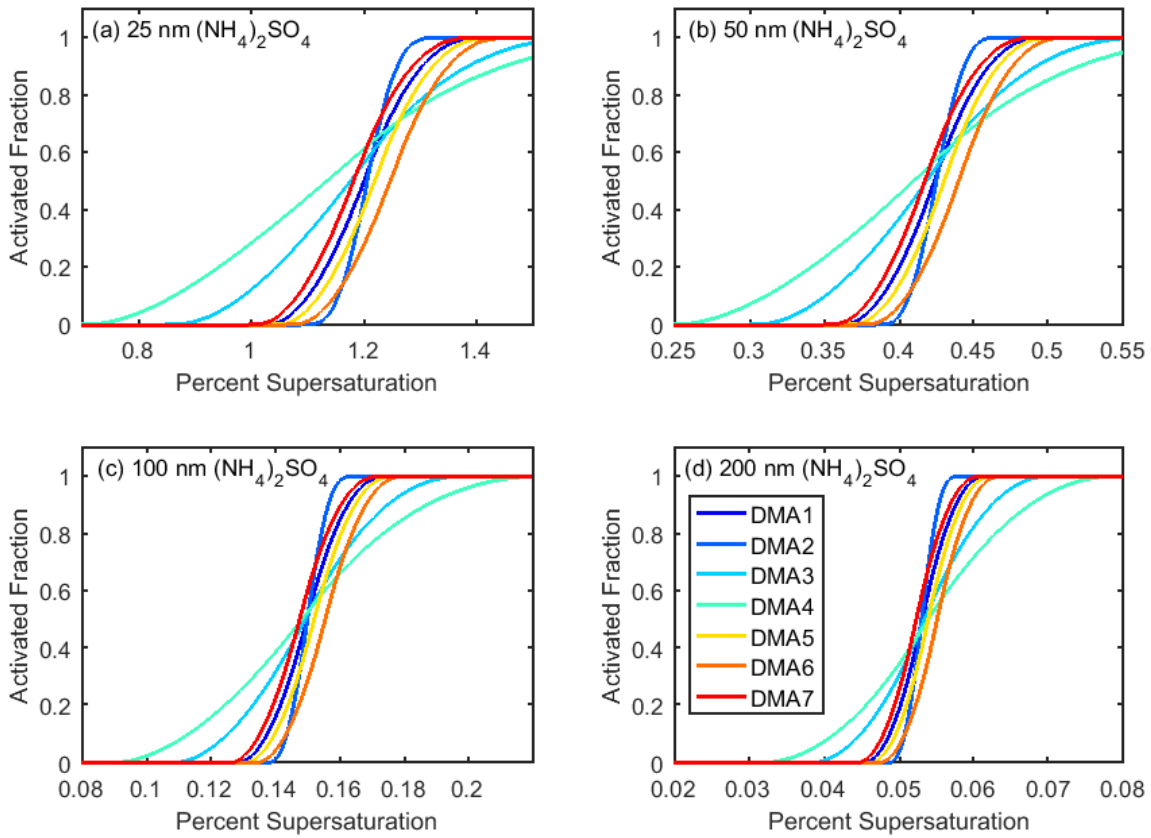


**Figure 10** Comparison of  $\kappa_{app}$  artifacts derived from best and worst Case scenarios for instrumental measurements for sodium chloride. Combined artifacts for the lowest-artifact Cases (Best: DMA Case 2, CPC Case 3, and CCN Case 4) and the highest-artifact Cases (Worst: DMA Case 4, multiple charging, CPC Case 4, CPC Case 8, and CCN Case 1).



Added Figure S2 Exemplary  $(NH_4)_2SO_4$  CCN activation curves for DMA Cases 1-7.

- 3) **Reviewer comment:** Regarding my formed general comment 3: I think one would like to see a more quantitative analysis of the uncertainties of kappa after taking the influence of instrument calibration by a standard compound into account. This is most relevant to real CCN measurement and is most interesting to those who do the measurement and who use these data. I also suggest that the discussion should be somewhat included in the conclusion because if after the calibration using (NH<sub>4</sub>)<sub>2</sub>SO<sub>4</sub> or NaCl, the discrepancy caused by instrument artifacts would be much smaller than values shown in the manuscript.

**Authors' response:** As the Reviewer points out, accuracy in measurements depend on accurate calibrations. In this case, accurate determination of the supersaturation setpoints within the CCN instrument are dependent on accurate sizing of aerosols entering the CCN, and therefore are dependent on the DMA sizing during CCN calibration. CCN calibrations during two standard compounds, ammonium sulfate and sodium chloride, as described in detail in Rose (2008). Fortunately, if the calibration procedure described by Rose is followed and an optimal DMA aerosol to sheath ratios employed, the uncertainties will be minimal. Specifically, our analysis shows that an aerosol to sheath ratio of 1:10 or 1:20 (Case 1 or 2, respectively) is recommended for all CCN calibrations. This will result in kappa uncertainties of less than 1% for all dry sizes (25 to 200 nm). However, if CCN calibrations are performed using a DMA operated with less than ideal aerosol to sheath ratios, substantial errors will be introduced. Analysis of the impact of DMA uncertainties on CCN calibrations are discussed in detail in the Supplemental Materials. In the worst case scenario amongst the cases evaluated here (Case 4), the resulting uncertainty in apparent kappa is 15%.

Details of the assessment of impacts of DMA sizing on CCN calibration follow:

We have now assessed the effects of calibration with a standard compound on subsequent CCN measurements, given that the DMA flow settings used in the calibration are the same as those used for subsequent measurements. Calibration with a standard will yield new parameters, *A* and *B*, for a linear equation that relates percent supersaturation, %*SS*, to the change in temperature set by the instrument,  $\Delta T_{set}$ :

$$\Delta T_{set} = (A \times \%SS) + B$$

If the slope *A* and/or y-intercept *B* are inaccurate, the instrument will choose  $\Delta T_{set}$  incorrectly for input percent supersaturation values. In order to model this error, the  $\kappa$ -Köhler theory %*SS*<sub>crit</sub> for 25, 50, 100, and 200 nm ammonium sulfate and sodium chloride was used to determine the “correct”  $\Delta T_{set}$  for the CCNC, using parameters *A* and *B* from a previous CCNC calibration in our lab. These  $\Delta T_{set}$  were then paired with the %*SS*<sub>crit</sub> for DMA Cases 1-7 determined in Section 3.1.2  $\kappa_{app}$  artifacts arising from DMA flow ratios, as shown in Figure S3. A linear regression was run for each composition and DMA Case to

find new parameters  $A$  and  $B$ . For clarity, the original  $\Delta T_{set}$  equation with the original parameters  $A_0$  and  $B_0$  will hereon be referred to as Eq. S1, and the new  $\Delta T_{set}$  equations for each DMA Case  $C$  with new parameters  $A_C$  and  $B_C$  will be referred to as Eq. S2.

$$\Delta T_{set} = (A_0 \times \%SS) + B_0 \quad (S1)$$

$$\Delta T_{set} = (A_C \times \%SS) + B_C \quad (S2)$$

For each composition (sodium chloride or ammonium sulfate) and DMA Case, Eq. S2 was used to determine the  $\Delta T_{set}$  that the CCNC would set to achieve a series of percent supersaturations (0.01-1.5%). Then, Eq. S1 was used to determine the actual percent supersaturation that would result from each  $\Delta T_{set}$ . A few assumptions have been made so far: first, that the DMA aerosol/sheath ratio that was used during the calibration is also used in order to collect CCN activation data later, using the same compound; and second, that the original  $A_0$  and  $B_0$  used Eq. S1 were correct.

Two activated fraction curves were then plotted for each DMA Case (an example with DMA Cases 1-4 is shown in Figure S4). The activated fraction values for both curves were taken from the results in Section 3.1.2  $\kappa_{app}$  artifacts arising from DMA flow ratios. The accurate percent supersaturation values (dashed lines) were obtained from the original equation, and the observed percent supersaturation values (solid lines) are the values that would be reported by the CCNC according to the new equations.

Then,  $\%SS_{crit}$  was determined for each observed activated fraction curve, as shown in Fig. S5a. The apparent hygroscopicity  $\kappa_{app}$  was calculated for each DMA Case using Eq. 4, as shown in Fig. S5b. Apparent hygroscopicity artifacts are shown in Fig. S5c-d.

**Authors' changes to the manuscript:** Minor changes have been made to the text, and further details have been added to the supplemental information.

Pages 18-19 Lines 327-339 the text now reads: "In addition to the errors discussed above, accuracy in CCN measurements depend on the accuracy of the instrument calibration. Specifically, accurate determination of the percent supersaturation set points within the CCN instrument are dependent on accurate sizing of aerosols entering the CCN, and therefore are dependent on the DMA sizing during CCN calibration. CCN calibrations during two standard compounds, ammonium sulfate and sodium chloride, as described in detail in Rose (2008). Fortunately, if the calibration procedure described by Rose is followed and an optimal DMA aerosol to sheath ratios employed, the uncertainties will be minimal. Specifically, this analysis shows that an aerosol/sheath ratio of 1:10 or 1:20 (Case 1 or 2, respectively) is recommended for all CCN calibrations. This will result in  $\kappa_{app}$  uncertainties of less than 1%

for all dry sizes (25 to 200 nm). However, if CCN calibrations are performed using a DMA operated with less than ideal aerosol to sheath ratios, substantial errors will be introduced. Analysis of the impact of DMA uncertainties on CCN calibrations are discussed in detail in the Supplemental Materials. In the worst case scenario amongst the cases evaluated here (Case 4), the resulting uncertainty in  $\kappa_{app}$  is 15%.”

Pages 36 Lines 700-703 the text now reads: “By extension, the issue of uncertain sizing by the DMA leads to added uncertainties in the CCN instrument calibrations which are strongly dependent on the chosen aerosol to sheath ration within the DMA. We recommend conducting all CCN calibrations with DMA aerosol to sheath ratio of 1:10 or 1:20 which will reduce kappa uncertainties to less than 1% for all dry sizes (25 to 200 nm).”

In addition, Figures S3-S5 and the associated text have now been added to the Supplemental Materials.

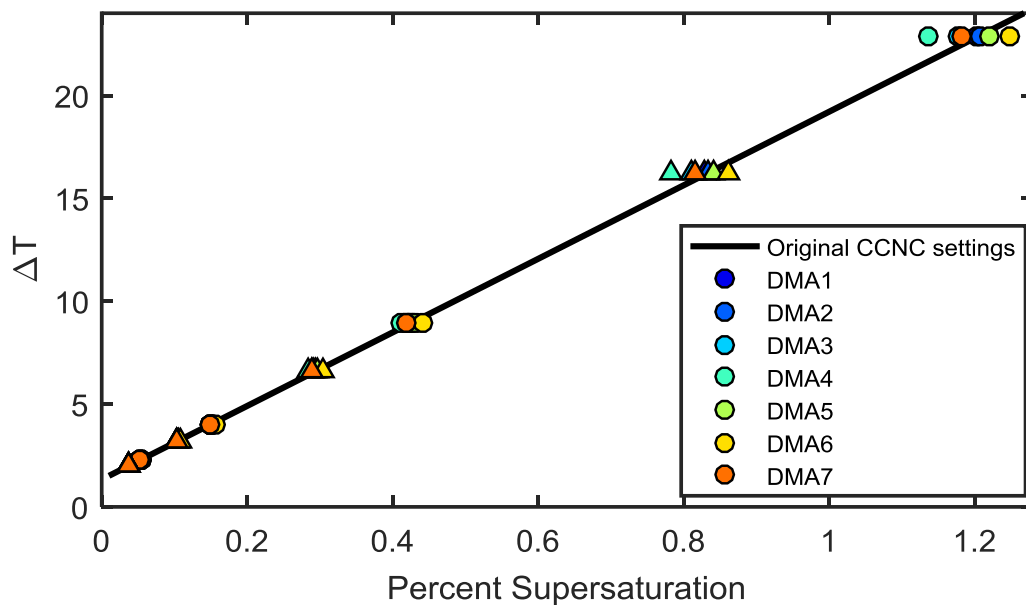


**Figure S3** CCN data used to determine new parameters during calibration.



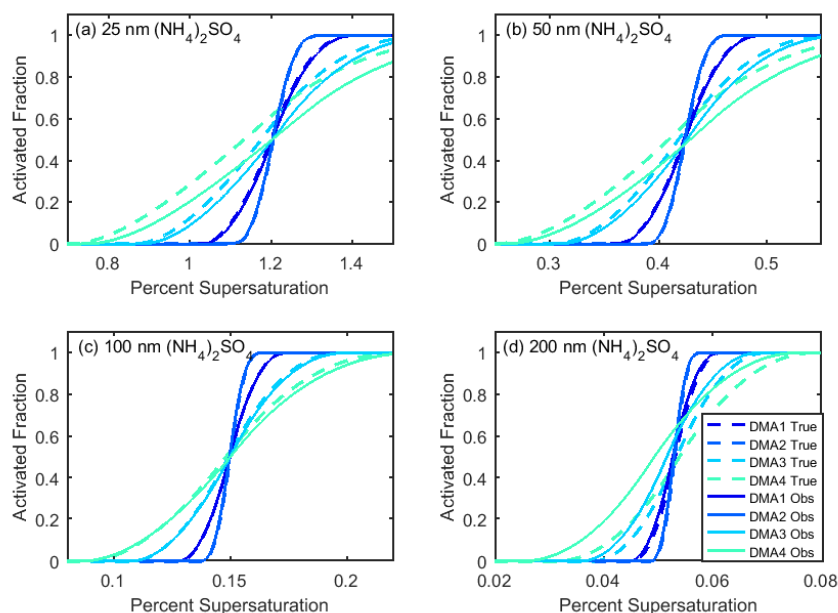


**Figure S4** Exemplary  $(\text{NH}_4)_2\text{SO}_4$  CCN activation curves for DMA Cases 1-7, resulting from inaccurate CCN instrument calibration. The true activation curve is shown with dashed lines, and the observed activation (inaccurate supersaturation reported by the instrument) is shown with solid lines.

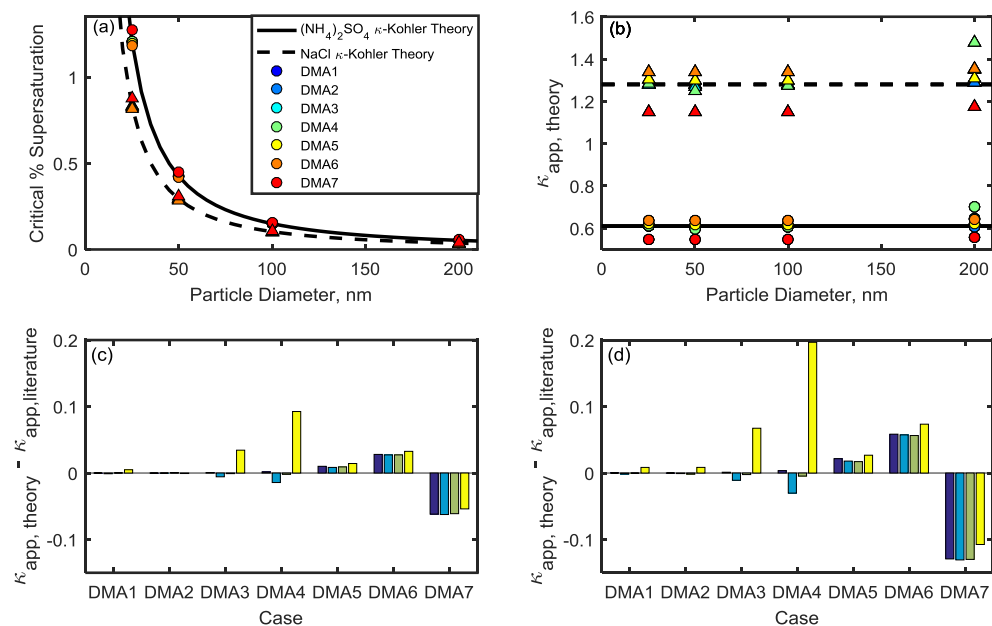


**Figure S5** (a) Critical supersaturation of ammonium sulfate and sodium chloride particles calculated for DMA Cases 1-7 for sodium chloride (triangles) and ammonium sulfate (circles), following calibration with the same DMA settings. Ammonium sulfate and sodium chloride curves from  $\kappa$ -Köhler theory are shown for comparison. (b) Apparent hygroscopicity  $\kappa_{app}$  for DMA Cases 1-7. (c) DMA-flow-derived artifacts in ammonium sulfate  $\kappa_{app}$  are shown for each DMA case. (d) DMA-flow-derived artifacts in sodium chloride  $\kappa_{app}$  are shown for each DMA case.

## Technical Comments

1. Reviewer comment: In figure 3a, in the lognormal distribution it is  $dN/d\log D_p$  that follows the shape of the curve rather than  $N$  (number concentration, y-axis) or  $dN/dD_p$ .

Authors' response: Our distribution represents the number concentration.

Authors' response to comments on "Instrument Artifacts Lead to Uncertainties in Parameterizations of Cloud Condensation Nucleation", Revised Submission, Referee #3

Authors' response: We thank the Reviewer for her/his feedback, which we feel have improved the manuscript.

Additional specific modifications are discussed below.

- 1) Reviewer comment: Line 98-Differences in reported  $\kappa_{app}$  values... 'ed' added

Authors' response: We thank the reviewer for finding this error.

Authors' changes to the manuscript: Page 6 Line 95 the text now reads: "Differences in reported  $\kappa_{app}$  values..."

- 2) Reviewer comment: Line 96-Differences in an aerosol's ability... 'an' added

Authors' response: We thank the reviewer for finding this error.

Authors' changes to the manuscript: Page 6 Line 99 the text now reads: "...rather any actual differences in an aerosol's ability..."

- 3) Reviewer comment: Line 643-Operating conditions: lowest DMA/sheath... 'colon and space issue'

Authors' response: We thank the reviewer for finding this error.

Authors' changes to the manuscript: Page 35 Lines 664-668 the text now reads: "The lowest combined artifacts ( $0.0021 < \kappa_{app,artifact} < 0.0074$ , NaCl) occurred as a result of ideal operating conditions: lowest DMA/sheath ratio, corrected multiple particle charging, and little to no undercounting."

- 4) Reviewer comment: The references are not spaced.

Authors' response: We thank the reviewer for finding this error.

Authors' changes to the manuscript: Spaces have been inserted between references.

- 5) Reviewer comment: Finally, the DMT CCN-100 can be operated under various flows from 200-900 cc/min although it is typically operated at 500 cc/min. The flow ratio (aerosol to

sheath) of the CCNC may also be altered but is typically set at 1:10. The paper should specify these details of operation.

Authors' response: We have added the recommended details to *Section 5. Artifacts derived from cloud condensation nuclei instruments*.

Authors' changes to the manuscript: Page 30 Lines 559-562 the text now reads: "The total flow through the DMT CCN-100 is 0.20-0.90 L min<sup>-1</sup>, though the instrument is typically operated with a total flow of 0.50 L min<sup>-1</sup>. The aerosol/sheath ratio in the DMT CCN-100 is set by the user, and a ratio of 1:10 is commonly chosen."

Rose, D., Gunthe, S. S., Mikhailov, E., Frank, G. P., Dusek, U., Andreae, M. O., and Poschl, U.: Calibration and measurement uncertainties of a continuous-flow cloud condensation nuclei counter (DMT-CCNC): CCN activation of ammonium sulfate and sodium chloride aerosol particles in theory and experiment, *Atmos. Chem. Phys.*, 8, 1153-1179, 10.5194/acp-8-1153-2008, 2008.

1 **Instrument Artifacts Lead to Uncertainties in Parameterizations of Cloud**

2 **Condensation Nucleation**

3 **Jessica A. Mirrielees and Sarah D. Brooks**

4 Texas A&M University, College Station, TX 77843

5 Correspondence E-mail: [jmirrieles@tamu.edu](mailto:jmirrieles@tamu.edu)

## 6 Abstract

7

8 The concentrations of cloud condensation nuclei (CCN) modulate cloud properties, rainfall  
9 location and intensity, and climate forcings. This work assesses uncertainties in CCN  
10 measurements and the apparent hygroscopicity parameter ( $\kappa_{app}$ ) which is widely used to represent  
11 CCN populations in climate models. CCN measurements require accurate operation of three  
12 instruments: the CCN instrument, the differential mobility analyzer (DMA), and the condensation  
13 particle counter (CPC). Assessment of DMA operation showed that varying the ratio of aerosol to  
14 sheath flow from 0.05 to 0.30 resulted in discrepancies between the  $\kappa_{app}$  values calculated from  
15 CCN measurements and the literature value. Discrepancies were found to increase from < 1% to  
16 13% for both sodium chloride and ammonium sulfate. The ratio of excess to sheath flow was also  
17 varied, which shifted the downstream aerosol distribution towards smaller particle diameters (for  
18 excess flow < sheath flow) or larger particle diameters (for excess flow > sheath flow) than  
19 predicted. For the CPC instrument, undercounting occurred at high concentrations, resulting in  
20 calculated  $\kappa_{app}$  lower than the literature values. Lastly, undercounting by CCN instruments at  
21 high concentration was also assessed, taking the effect of supersaturation on counting efficiency  
22 into account. Under recommended operating conditions, the combined DMA, CPC, and CCN  
23 uncertainties in  $\kappa_{app}$  are 1.2% or less for 25 to 200 nm diameter aerosols.

24 **Copyright Statement**

25 Will be provided by Copernicus.

## 26 1. Introduction

27

28 Aerosol-cloud interactions represent a major uncertainty in current predictions of the Earth's climate  
29 (IPCC, 2013). According to well-known Köhler theory, an aerosol's potential to catalyze cloud droplet  
30 formation by activating as a cloud condensation nucleus (CCN) depends on its physical and chemical  
31 properties. For any given composition, the CCN activation potential of an aerosol increases as its  
32 diameter decreases. While the relationship between aerosol diameter and CCN activation is  
33 straightforward, the effect of composition on an aerosol's ability to participate in cloud formation is  
34 more complex (Petters and Kreidenweis, 2013; Ovadnevaite et al., 2011). Predicting the cloud forming  
35 capacity of various air masses based on the properties of the aerosol they contain is essential for  
36 evaluating relative contributions from pollution, continental background and marine aerosol sources  
37 (Brooks and Thornton, 2018; Carslaw et al., 2013). Long-term CCN measurements are available from  
38 numerous locations globally (Schmale et al., 2018). However, understanding regional and temporal  
39 variability in CCN populations requires the ability to assess whether observed differences reflect true  
40 physical differences or simply variations in CCN sampling strategies.

41

42 Parameterizations of CCN activity which accurately prescribe CCN measurements are needed for  
43 climate models, cloud resolving models, and air quality predictions (Betancourt and Nenes, 2014;  
44 Betancourt et al., 2013; Chang et al., 2017; Crosbie et al., 2015; Karydis et al., 2012; Kawecki and  
45 Steiner, 2018). One parameterization was designed to represent the cloud droplet activation potential  
46 ambient aerosol masses of unknown composition with a single variable, kappa ( $\kappa$ ) based on the dry  
47 aerosol's hygroscopicity, or ability to uptake water and form a solution droplet (Petters and  
48 Kreidenweis, 2007). Various names and abbreviations have been given to  $\kappa$  throughout the literature:  
49 "hygroscopicity parameter", "single hygroscopicity parameter",  $\kappa$  (Petters and Kreidenweis, 2007;



50 Carrico et al., 2008; Asa-Awuku et al., 2010; Moore et al., 2012b); “CCN-derived  $\kappa$ ”,  $\kappa_{CCN}$  (Carrico et  
51 al., 2008; Petters and Kreidenweis, 2007); and the “apparent hygroscopicity parameter”  $\kappa_{app}$  (Sullivan  
52 et al., 2009; Collins et al., 2016; Petters and Kreidenweis, 2013). The term *apparent* hygroscopicity is  
53 favored by many because it emphasizes that fact that while CCN activation can often be predicted  
54 accurately by hygroscopic water uptake, they are different physical processes. It is possible for a  
55 compound to have high intrinsic hygroscopicity and low apparent hygroscopicity if it is poorly soluble  
56 in water (Sullivan et al., 2009).

57

58 Parameterizations of hygroscopicity that pre-date Petters and Kreidenweiss 2007 exist as well. Winkler  
59 1973 developed an equation for approximating the growth of an aerosol particle with relative humidity,  
60 based on the quantity and physical characteristics of the soluble species in the particle. Another  
61 approximation for the relationship between the equilibrium size of a particle and relative humidity was  
62 derived by Fitzgerald in 1975, in which the soluble fraction and composition of the soluble  
63 component(s) are taken into account. Fitzgerald et al., 1982 derived a particle composition parameter  
64 using the mass fraction and physical properties of soluble material in a particle. Kreidenweis et al., 2005  
65 determined that the critical activation diameter of dry aerosol particles can be calculated from simplified  
66 Köhler theory using the physical properties of water and the solute in a solution droplet. This  
67 parameterization has been used in CCN closure studies (Bougiatioti et al., 2009; Moore et al., 2011;  
68 Moore et al., 2012a). The earliest prediction of CCN concentrations for specific particle diameters and  
69 hygroscopicity used this parameterization as well (Mochida et al., 2006).

70

71 Once calculated, hygroscopicity parameters are useful tools for comparing CCN field measurements  
72 conducted in various regions and seasons and for making predictions about cloud formation, aerosol-  
73 cloud interactions in weather, and climate models. Values of  $\kappa_{app}$  can be used to compare the CCN

74 results in field and laboratory studies, including sea spray aerosol. For example, aggregation of results  
75 from several mesocosm experiments and marine field studies found submicron (30-100 nm)  $\kappa_{app}$  for sea  
76 spray aerosol as low as 0.4 and as high 1.3 (Collins et al., 2016). Another study, which included a  
77 survey of observational CCN data, reported that marine and continental aerosols could be described by  
78  $\kappa_{app}$  values of  $0.7 \pm 0.2$  and  $0.3 \pm 0.1$  respectively (Andreae and Rosenfeld, 2008).

79  
80 Several studies have examined the sensitivity of models to  $\kappa$  values derived from HTDMA  
81 measurements. An analysis of the NASA Global Modeling Initiative Chemical Transport Model and the  
82 GEOS-Chem CTM (Karydis et al., 2012) found that cloud droplet number concentration is sensitive to  $\kappa$   
83 in Arctic and remote regions, where background aerosol loadings are low. Another study (Betancourt  
84 and Nenes, 2014) found that a  $\pm 50\%$  uncertainty range in the  $\kappa$  of secondary organic aerosols and  
85 particulate organic matter resulted in a cloud droplet number concentration uncertainty of up to 15 %  
86 and 16 %, respectively. Updating precipitation models with lab-derived  $\kappa$  values for specific inorganic  
87 and organic species may increase the accuracy of storm forecasts by providing better predictions of  
88 intense precipitation (Kawecki and Steiner, 2018). In terms of climate, (Liu and Wang, 2010) found that  
89 increasing the  $\kappa$  of primary organic aerosols from 0 to 0.1, and decreasing the  $\kappa$  of secondary organics  
90 aerosols from 0.14 to 0.07, resulted in an uncertainty in global secondary aerosol indirect forcing of 0.4  
91  $\text{Wm}^{-2}$  from pre-industrial times to present day.

92  
93 The sensitivity of weather and climate models to hygroscopicity parameters demonstrates the need for  
94 accurate measurements. In this study, we examine experimental uncertainties in CCN measurements and  
95 the resulting uncertainties in determination of  $\kappa_{app}$ . Differences in reported  $\kappa_{app}$  values may result  
96 from experimental artifacts rather than actual differences in an aerosol's ability to facilitate cloud  
97 formation. By systematically quantifying sources of experimental error, this study provides a

- 98 framework for determining the significance of variations in CCN properties reported in multiple studies
- 99 and defining the operating conditions which minimize instrumental artifacts.

## 100 2. Background

101

102 The Köhler equation relates water vapor saturation ratio at the surface of a wet droplet,  $s$ , to its radius at  
103 equilibrium (Rogers and Yau, 1989):

104

$$105 \quad s = \left(1 - \frac{b}{r^3}\right) \exp\left(\frac{a}{r}\right) \quad (1a)$$

106

$$107 \quad a = \frac{2\sigma_w M_w}{\rho_w R T} \quad (1b)$$

108

$$109 \quad b = \frac{3im_s M_w}{4\pi\rho_w M_s} \quad (1c)$$

110

111 where  $s$  is the equilibrium saturation ratio of a solution droplet with radius  $r$ ,  $\sigma_w$  is the surface tension of  
112 water,  $M_w$  is the molecular weight of water,  $R$  is the ideal gas constant,  $T$  is temperature in Kelvin,  $\rho_w$  is  
113 the density of water, and  $M_s$  is the molecular weight of the solute. The minimum saturation ratio that is  
114 required for spontaneous droplet growth,  $s_{act}$ , is therefore:

115

$$116 \quad s_{crit} = 1 + \sqrt{\frac{4a^3}{27b}} \quad (2)$$

117

118 Petters and Kreidenweis [2007] reformulated the Köhler equation as  $\kappa$ -Köhler theory:

119

$$120 \quad s_{crit} = \exp\left(\sqrt{\frac{4A^3}{27D_{act}^3 \kappa_{app}}}\right) \quad (3a)$$

121 and

122

123

$$A = \frac{4\sigma_{lv}M_w}{RT\rho_w} \quad (3b)$$

124

125 Where  $s_{crit}$  is the critical water vapor saturation ratio,  $D_{act}$  is the dry particle activation diameter and

126  $\kappa_{app}$  is the apparent hygroscopicity parameter. Solving for  $\kappa_{app}$  yields:

127

128

$$\kappa_{app} = \frac{4A^3\sigma_{lv}^3}{27T^3D_{act}^3\ln^2(s_{crit})} \quad (4)$$

129

130 The apparent hygroscopicity parameter can be calculated from experimental CCN results, where the dry

131 diameter and water vapor saturation ratio are known. For a chosen aerosol diameter, the activated

132 fraction is the ratio of the concentration aerosols that activate as CCN to the total aerosol concentration:

133

134

$$\textit{Activated fraction} = \frac{\textit{CCN Concentration}}{\textit{Aerosol Concentration}} \quad (5)$$

135

136 Activated fraction data is fit with a sigmoid error function to determine the percent supersaturation at

137 which 50 % of the particles have activated as CCN (activated fraction = 0.50), which is considered the

138 operationally defined critical percent supersaturation  $SS_{crit}$  (Rose et al., 2008). The critical saturation

139 ratio  $s_{crit}$  can then be determined and entered into Eq. (4) in order to calculate  $\kappa_{app}$  for the near-

140 monodisperse aerosol:

141

142

$$s_{crit} = 1 + \frac{SS_{crit}}{100} \quad (6)$$

143

144 Reporting  $\kappa_{app}$  as a function of diameter allows for the comparison of the cloud condensation nucleation  
145 abilities of multimodal aerosol populations, without overlooking differences which arise due to aerosol  
146 composition.

147

148 The apparent hygroscopicity parameter is related to chemical composition; therefore, the calculated  $\kappa_{app}$   
149 of a pure substance should be constant across CCN experiments. However, discrepancies between  $\kappa_{app}$   
150 for a single chemical species have been observed. Experimental results for ammonium nitrate are  
151 inconsistent with reported values ranging from  $0.577 \leq \kappa_{app} \leq 0.753$  (Svenningsson et al., 2006).

152 Also, large ranges are often observed for organic compounds, such as glutaric acid ( $0.054 \leq \kappa_{app} \leq$   
153  $0.16$ ) and malonic acid ( $0.199 \leq \kappa_{app} \leq 0.255$ ) (Koehler et al., 2006; Kumar et al., 2003; Hartz et al.,  
154 2006). Below we evaluate potential sources of uncertainties in CCN measurements and the resulting  
155 uncertainties in  $\kappa_{app}$ .

156

### 157 **3. Artifacts derived from sized CCN measurements**

158

159 CCN measurements used for calculating apparent hygroscopicity from monodisperse aerosol require  
160 accurate operation of three instruments: the CCN, the differential mobility analyzer (DMA), and the  
161 condensational particle counter (CPC). The setup for laboratory CCN experiments is shown in Fig. 1.  
162 First, a polydisperse population of aerosols is generated by an atomizer and dried using a desiccant tube  
163 packed with silica gel. A near-monodisperse flow is obtained through size-selection in the DMA. The  
164 flow is then split between a CPC (which measures aerosol concentration) and a CCN counter (which  
165 measures the concentration of particles that activate as cloud condensation nuclei at a given percent  
166 supersaturation). Instrument artifacts will first be assessed separately for the DMA, CPC, and CCN  
167 counter. In the concluding section of the paper (and Fig. 10), the overall uncertainty due to the  
168 combination of these is presented and discussed.

169

170 We note that this study considers sized CCN measurements which may be used for the determination of  
171  $\kappa_{app}$ . In contrast, a number of earlier CCN studies conducted on the full ambient aerosol population  
172 without sizing the aerosol (Jennings et al., 1996; Hudson and Xie, 1998; Modini et al., 2015; Duan et al.,  
173 2017; Schmale et al., 2018; Leng et al., 2013). While useful, such studies do not produce the data  
174 required for accurate determination of  $\kappa_{app}$  from the CCN measurements.

175

#### 176 **3.1 Artifacts derived from differential mobility analyzers**

177

##### 178 **3.1.1 DMA operation and electrical mobility**

179

180 Differential mobility analyzers used in atmospheric science include commercially available instruments  
 181 from Grimm Aerosol Technik, TSI Incorporated, and MSP Corporation. They have also been custom  
 182 built by a number of research groups (Mei et al., 2011;Barmounis et al., 2016;Jokinen and Makela,  
 183 1997;Seol et al., 2000). All models allow for the selection of particles through electrical mobility, the  
 184 ability of a particle to move through a medium (such as air) while acted upon by an electrical field. The  
 185 DMA size-selects near-monodisperse aerosol from a polydisperse aerosol source, as shown in Fig. 2  
 186 (modeled after the Vienna-type long Differential Mobility Analyzer from Grimm Technologies). The  
 187 electrical mobility  $Z_p$  of a particle with mobility diameter  $d_m$  can be calculated according to:

188

$$189 \quad Z_p = \frac{neC_C(d_m)}{3\pi\eta d_m} \quad (7)$$

190

191 where  $n$  is the number of charges on the particle (assumed to be one in this study),  $e$  is the elementary  
 192 unit of charge,  $\eta$  is the gas dynamic viscosity, and  $C_C(d_m)$  is the Cunningham slip correction factor:

193

$$194 \quad C_C(d_m) = 1 + \frac{2\lambda}{d_m} \left( \alpha_{CC} + \beta_{CC} \exp \left[ -\frac{\gamma_{CC}}{2\lambda/d_m} \right] \right) \quad (8)$$

195

196 where  $\lambda$  is the mean free path (DeCarlo et al., 2004). For the Vienna-type long Differential Mobility  
 197 Analyzer from Grimm Technologies, Inc. considered here,  $\alpha_{CC} = 1.246$ ,  $\beta_{CC} = 0.42$ , and  $\gamma_{CC} = 0.86$   
 198 (Grimm Aerosol Technik, 2009).

199

200 Particle-laden flow enters the differential mobility analyzer through the aerosol inlet (flow  $Q_a$ ), and travels  
 201 down the DMA column (inner radius  $r_1$ , outer radius  $r_2$ ) with the clean air sheath flow  $Q_{sh}$ . Positively-  
 202 charged particles are attracted by the negatively-charged inner electrode, to which voltage  $V_0$  has been



203 applied. Ideally, selection of a voltage allows only particles of a specific mobility diameter to exit the  
 204 DMA through the sample flow  $Q_s$ . All particles with larger diameter (lower  $Z_p$ ) or smaller diameter  
 205 (higher  $Z_p$ ) will exit the DMA through the excess flow  $Q_e$ . In other words,  $Q_s$  would ideally consist only  
 206 of aerosols with diameters equal to, or very nearly equal to, the selected diameter.

207

208 In reality, the aerosol flow that leaves the DMA through  $Q_s$  is polydisperse with a mobility distribution  
 209 determined by instrumental parameters. A triangular approximation has been chosen as a model for this  
 210 distribution, as particle inertia is negligible for the diameters considered in this study (Stratmann et al.,  
 211 1997; Mamakos et al., 2007). The probability that a particle at the aerosol inlet will exit with the sampling  
 212 flow is defined by transfer function  $f(Z_p, Z_{p,mid})$ :

213

$$214 \quad f(Z_p, Z_{p,mid}) = \frac{\alpha_{TF}}{2\beta_{TF}} \left( \left| \frac{Z_p}{Z_{p,mid}} - (1 + \beta_{TF}) \right| + \left| \frac{Z_p}{Z_{p,mid}} - (1 - \beta_{TF}) \right| - 2 \left| \frac{Z_p}{Z_{p,mid}} - 1 \right| \right) \quad (9)$$

215 where  $Z_{p,mid}$  is the midpoint mobility of the transfer function, and  $\alpha_{TF}$  and  $\beta_{TF}$  are flow-derived  
 216 constants, defined as:

217

$$218 \quad \alpha_{TF} = \frac{Q_s + Q_a}{2Q_a} \quad (10a)$$

219 and

$$220 \quad \beta_{TF} = \frac{Q_s}{Q_{sh}} \quad (10b)$$

221

222 The midpoint and half-width of the transfer function are respectively calculated according to: (Knutson  
 223 and Whitby, 1975)

$$224 \quad Z_{p,mid} = \frac{Q_e + Q_{sh}}{4\pi LV_0} \ln \left( \frac{r_2}{r_1} \right) \quad (11a)$$

225 and

226

$$227 \quad \Delta Z_p = \frac{Q_a}{2\pi LV_0} \ln\left(\frac{r_2}{r_1}\right) \quad (11b)$$

228

229 where L is the distance between the DMA inlet and outlet.

230

### 231 **3.1.2 $\kappa_{app}$ artifacts arising from DMA flow ratios**

232

233 Next we assess the ramifications of the DMA transfer function for the derived  $\kappa_{app}$ . A lognormal  
234 theoretical aerosol number distribution was used to represent a polydisperse ambient aerosol population  
235 (Fig. 3a). This distribution was converted to an electrical mobility distribution using Eq. (7) and Eq. (8),  
236 assuming that the aerosols in the distribution were spherical and singly charged. From the distribution, a  
237 series of single aerosol sizes were selected (25, 50, 100, and 200 nm diameter). For each aerosol size,  
238 the resulting DMA transfer functions were calculated for seven cases using Eq. (9) and the various  
239 parameters for DMA sheath, excess, aerosol, and sample flow listed in Table 1. These seven cases were  
240 chosen to represent possible measurements scenarios that may be encountered in a CCN experiment.  
241 The aerosol/sheath ratio is varied in Cases 1-4 in order to study the effects of chosen experimental  
242 parameters. Sheath flow is predetermined in some DMAs (for example, the Grimm Vienna DMA  
243 considered in this study), but can be varied in other instruments. The aerosol flow rate may also be  
244 selected in an experiment. Cases 5-7 vary the excess/sheath ratio in order to take proper instrument  
245 operation into account. The excess and sheath flow should be identical, but small discrepancies may  
246 occur.

247

248 For example, the resulting DMA transfer functions for a 100 nm aerosol conditions constrained by Cases  
249 1-4 are shown in Fig. 3b, where an increase in  $Q_a/Q_{sh}$  from 0.1 (black line) to 0.3 (green line) tripled  
250 the width of the number distribution, and decreasing  $Q_a/Q_{sh}$  to 0.05 (blue line) from 0.10 halved the  
251 width of the number distribution. The result of applying the transfer functions shown in Fig. 3b to the  
252 distribution in Fig. 3a is shown in Fig. 3c.

253

254 All downstream distributions for all seven DMA cases and all aerosol sizes are shown in Fig. S1 in the  
255 Supplement. DMA Cases 1-4 represent experimental conditions in which the sheath and excess air  
256 flows are equal and the aerosol/sheath flow ratio is varied. As  $Q_a/Q_{sh}$  increases, the width of the  
257 number distribution measured downstream of the DMA increases, while the midpoint diameter remains  
258 constant. It was found that doubling the aerosol to sheath ratio doubled the width of the downstream  
259 number distribution for 25, 50, 100, and 200 nm particles. For example, when selecting 200 nm  
260 particles, increasing  $Q_a/Q_{sh}$  from 0.10 to 0.20 increased the downstream diameter range from 181-222  
261 nm (a spread of 41 nm) to 167-250 nm (a spread of 87 nm). The particle diameter ranges that would be  
262 observed downstream of the DMA are summarized in Table 2.

263

264 To assess the variations in CCN properties resulting from DMA uncertainties the critical percent  
265 supersaturation were calculated for representative atmospheric aerosols. The value of  $SS_{crit}$  was  
266 calculated for each particle diameter using Eq. (3a), using literature values for apparent hygroscopicity  
267 of 0.61 for ammonium sulfate and 1.28 for sodium chloride (Clegg et al., 1998). It should be noted that  
268 this analysis considers two homogeneous aerosol distributions of hygroscopic salts. Real aerosol  
269 distributions tend to be mixtures of many species, and the shape of the number distribution can vary  
270 between species.

271

272 To test how uncertainties in DMA diameter translate to uncertainties in  $\kappa_{app}$ , the activation of particles  
 273 downstream of the DMA was assessed. First, for each case and diameter (25, 50, 100, and 200 nm) the  
 274 critical saturation ratio  $s_{crit}$  was calculated for each particle diameter range downstream from the DMA  
 275 using Eq. 3a. These critical saturation ratios were converted to critical percent supersaturation  $SS_{crit}$   
 276 and used to calculate the activated fraction  $AF$  for the aerosol particles downstream from the DMA for  
 277 percent supersaturations  $0.01 < SS < 1.5$ , using the equation:

278

$$279 \quad AF = \frac{1}{2} \left( 1 + \operatorname{erf} \left( \frac{SS - SS_{crit}}{\sigma \sqrt{2}} \right) \right) \quad (12)$$

280

281 where the standard deviation  $\sigma$  was equal to one-hundredth of  $SS_{crit}$ . The small  $\sigma/SS_{crit}$  ratio was  
 282 chosen in order to generate accurate activated fraction curves for each particle diameter.

283

284 The activated fraction curve for each selected diameter (25, 50, 100, and 200 nm) was then calculated as  
 285 the sum of the number-weighted activated fractions of each particle diameter downstream from the  
 286 DMA. For example, for a selected diameter of 25 nm, the downstream diameters ranged from 23 nm to  
 287 27 nm for DMA Case 1 and from 20 nm to 36 nm in DMA Case 4. The equation used for this  
 288 calculation is:

289

$$290 \quad AF_{weighted} = \sum_i \frac{n_i}{n_{total}} AF_i \quad (13)$$

291

292 where  $AF_i$  is the activated fraction calculated using Eq. 12 and  $\frac{n_i}{n_{total}}$  is the fraction of particle  
 293 downstream from the DMA of diameter  $i$ .

294

295 This calculation was repeated for each selected diameter (25, 50, 100, and 200 nm), each DMA Case (1-  
296 7), and percent supersaturation (0.01-1.5) in order to construct activation curves for each selected  
297 diameter and DMA Case. As an example, in Fig. S2, the shape and position of each activated fraction  
298 curve vary with the DMA flow ratios. As the aerosol/sheath ratio increases, the activated fraction curve  
299 flattens out (DMA Case 4). The critical percent supersaturation  $SS_{crit}$  was then determined for each  
300 activation curve as the percent supersaturation where  $AF = 0.50$ . These results are shown in Fig. 4a  
301 for ammonium sulfate and sodium chloride. Eq. 4 was then used to calculate  $\kappa_{app,theory}$  for each DMA  
302 Case and selected diameter, as shown in Fig. 4b. Discrepancies between  $\kappa_{app,theory}$  calculated in this  
303 study and literature values (hereon referred to as “ $\kappa_{app}$  artifacts”) are shown for both compounds in Fig.  
304 4c-d.

306 The largest  $\kappa_{app}$  artifact was found in DMA case 4 (where the aerosol/sheath ratio was the highest) for  
307 both ammonium sulfate and sodium chloride aerosols. The artifacts for 25 nm ammonium sulfate  
308 aerosol in DMA case 4 was 0.08, or ~13% of the literature value used for  $\kappa_{app}^{(NH_4)_2SO_4}$ , while the artifacts  
309 for 25 nm sodium chloride in DMA case 4 was 0.16, or ~13% of the literature value used for  $\kappa_{app}^{NaCl}$ .  
310 Artifacts were also high for DMA case 6 ( $-0.041 \leq \kappa_{app,artifact}^{(NH_4)_2SO_4} \leq -0.048$ ) and DMA case 7  
311 ( $0.014 \leq \kappa_{app,artifact}^{(NH_4)_2SO_4} \leq 0.024$ ), where sheath and excess flow were unequal. This result demonstrates  
312 that artifacts may still occur when low aerosol/sheath flow ratios are chosen (0.15 and 0.08 for DMA  
313 cases 6 and 7, respectively) due to small differences between sheath and excess flow rates (5% and 2%  
314 for DMA cases 6 and 7, respectively).

315

316  $\kappa_{app}$  artifacts were larger for sodium chloride ( $-0.10 \leq \kappa_{app,artifact}^{NaCl} \leq 0.16$ ) than for ammonium  
317 sulfate ( $-0.05 \leq \kappa_{app,artifact}^{(NH_4)_2SO_4} \leq 0.08$ ) across the DMA cases. As our results show, when two or more  
318 compounds are compared, the more hygroscopic compound will have larger  $\kappa_{app}$  artifacts.

319  
320 This analysis was also applied to the range of apparent hygroscopicity values Svenningsson et al., 2006  
321 reported for ammonium nitrate  $0.577 \leq \kappa_{app} \leq 0.753$ , with a mean value of 0.670. If 0.670 is  
322 assumed to be the true  $\kappa_{app}$  for ammonium nitrate, then the sample/sheath ratio used to determine  $\kappa_{app}$   
323 (1.2-2.0 L min<sup>-1</sup>) could lead an experimental kappa as low as 0.665 or as high as 0.674, which would not  
324 fully explain the actual experimental range. This assessment ignores possibility of under/over counting  
325 which could introduce additional errors.

326  
327 In addition to the errors discussed above, accuracy in CCN measurements depend on the accuracy of the  
328 instrument calibration. Specifically, accurate determination of the percent supersaturation set points  
329 within the CCN instrument are dependent on accurate sizing of aerosols entering the CCN, and therefore  
330 are dependent on the DMA sizing during CCN calibration. CCN calibrations during two standard  
331 compounds, ammonium sulfate and sodium chloride, as described in detail in Rose (2008). Fortunately,  
332 if the calibration procedure described by Rose is followed and an optimal DMA aerosol to sheath ratios  
333 employed, the uncertainties will be minimal. Specifically, this analysis shows that an aerosol/sheath  
334 ratio of 1:10 or 1:20 (Case 1 or 2, respectively) is recommended for all CCN calibrations. This will  
335 result in  $\kappa_{app}$  uncertainties of less than 1% for all dry sizes (25 to 200 nm). However, if CCN  
336 calibrations are performed using a DMA operated with less than ideal aerosol to sheath ratios,  
337 substantial errors will be introduced. Analysis of the impact of DMA uncertainties on CCN calibrations

338 are discussed in detail in the Supplemental Materials. In the worst case scenario amongst the cases  
339 evaluated here (Case 4), the resulting uncertainty in  $\kappa_{\text{app}}$  is 15%.

340

### 341 **3.1.3 Effect of double and triple charges on particles**

342

343 During normal operation, the Grimm DMA employs a bipolar charger (also known as a neutralizer) to  
344 charge aerosol particles through the capture of gaseous ions. The analysis in Section 3.1.2 assumes that  
345 each particle carries a single (+1) charge. In reality, the methods used to charge particles prior to  
346 entering a DMA may impart two, three, or more charges to individual particles (Fuchs, 1963). The  
347 charge distribution resulting from a bipolar charger is roughly approximated using the Boltzmann law  
348 (Keefe et al., 1959). However, the Boltzmann law assumes symmetric aerosol particle charging (equal  
349 concentrations of negatively and positively charged particles). Deviation from symmetric charging is  
350 observed in regions of high ionizations, and this deviation becomes more pronounced as particle size  
351 increases (Hoppel and Frick, 1990). A more accurate estimation of stationary charge distribution has  
352 been calculated using an approximation formula for the charge distribution produced by a bipolar  
353 charger:

354

$$355 \quad f(k) = 10^{\left[\sum_{i=0}^{i=5} a_i(k) (\log_{10} D_{nm})^i\right]} \quad (14)$$

356

357 where  $f(k)$  is the fraction of particles carrying  $k$  charges,  $a_i(k)$  are approximation coefficients  
358 determined using a least-squares regression analysis, and  $D_{nm}$  is the particle diameter in nanometers  
359 (Wiedensohler, 1988). The approximation coefficients only apply to particles with 0,  $\pm 1$ , and  $\pm 2$   
360 charges. In a separate study, Maricq et al., 2008 determined approximation coefficients for poly ( $\alpha$ -  
361 olefin) oligomer oil droplets with  $\pm 1$ ,  $\pm 2$ , and  $\pm 3$  charges. The approximation coefficients reported by

362 these two studies were in excellent agreement for particles with  $\pm 1$  and in weak agreement for  $\pm 2$   
 363 charges (+2 and -2 charging efficiencies were overestimated by 50% and 100%, respectively).  
 364 Therefore, this analysis will use the approximation coefficients from Wiedensohler, 1988 for particles  
 365 with +1 and +2 charges, and the approximation coefficient for particles with +3 charge from Maricq et  
 366 al., 2008.

367  
 368 In order to assess the impact of multiple charges on  $\kappa_{app}$ , Eq. (14) and the approximation coefficients  
 369 from Wiedensohler, 1988 and Maricq et al., 2008 were used to calculate the charge distribution of the  
 370 representative aerosol population shown in Fig. 3a. The resulting charge distribution is shown in Fig.  
 371 S6a. An increase in multiple charging is observed as particle diameter increases, though this is offset  
 372 somewhat by the decrease in concentration with particle size above 50 nm.

373  
 374 It follows that aerosols incorrectly sized due to double and triple charging will be passed from the DMA  
 375 to the CCN and result in an additional uncertainty in the CCN measurements. To illustrate this, activated  
 376 fraction curves, were generated for 25, 50, 100, and 200 nm sodium chloride particle selection by the  
 377 DMA (Fig. 5). The activation of sodium chloride is represented by sigmoid curves, where the midpoint  
 378 of each activation curve is the  $\kappa$ -Köhler-derived critical supersaturation of sodium chloride, and the  
 379 standard deviation of each curve is one-tenth of this value (consistent with the standard  
 380 deviation/midpoint ratio observed from our instrument's ammonium sulfate CCN calibration data). For  
 381 each particle diameter,  $D$ , the observed activated fraction,  $AF_{D,weighted}^{SS}$ , for each percent supersaturation  
 382  $SS$  was determined by weighting the activated fraction  $AF_{D,i}^{SS}$  of each particle diameter/charge at that  
 383 percent supersaturation, by the fraction of particles of that diameter:

384  
 385 
$$AF_{D,weighted}^{SS} = \sum_{i=1}^{i=3} \frac{\text{concentration of particles with charge } i \text{ and diameter } D}{\text{concentration of particles with charge } +1, +2, +3, \text{ and diameter } D} AF_{D,i}^{SS} \quad (15)$$



386

387 The raw data shown in Fig. 5 (green curves) can be corrected for multiple charging by determining the  
388 fraction of particles with  $> +1$  charge from the lower plateau in each plot (dashed lines). The adjusted  
389 activated fraction for each percent supersaturation,  $AF_{adjusted}$ , is calculated using the equation:

390

$$391 \quad AF_{adjusted} = \frac{AF_{raw} - AF_{plateau}}{1 - AF_{plateau}} \quad (16)$$

392

393 where  $AF_{raw}$  is the raw activated fraction at that percent supersaturation, and  $AF_{plateau}$  is the activated  
394 fraction corresponding to the lower plateau (Rose, 2008). The adjusted activated fraction curves are  
395 shown in Fig. 5 (blue curves). These are in good agreement with the theoretical  $\kappa$ -Köhler-derived  
396 activation curves for sodium chloride (not shown).

397

398 Critical supersaturation was determined for each diameter by calculating the percent supersaturation at  
399 which the raw  $AF_{D,weighted}^{SS} = 0.5$ . These critical supersaturations are shown in Fig. 6a, and the  
400 theoretical critical supersaturations calculated from  $\kappa$ -Köhler theory are shown for comparison. Eq. 4  
401 was used to calculate apparent hygroscopicity for each particle diameter, shown in Fig. 6b. A dashed  
402 line in Fig. 6b indicates the literature value for  $\kappa_{app}^{NaCl}$ . It is apparent that failing to account for multiply-  
403 charged particle in the activated fraction curves shown in Fig. 5 leads to an overestimation of  $\kappa_{app}$ .

404 Artifacts in  $\kappa_{app}$  are shown in Fig. 6c.

405

406 For the theoretical aerosol distribution used in this analysis (Fig. 3a), small, positive deviations from  $\kappa$ -  
407 Köhler theory and the literature value for  $\kappa_{app}^{NaCl}$  were observed ( $0.01 \leq \kappa_{app,artifact}^{NaCl} \leq 0.04, 1 -$   
408  $3\%$  of  $\kappa_{app}^{NaCl}$ ). As shown in the figure,  $\kappa_{app}$  artifacts resulting from unaccounted-for multiple charges

409 decrease with particle diameter for this theoretical aerosol population. Greater  $\kappa_{app}$  artifacts would be  
410 expected for aerosol populations with more prevalent accumulation modes.

411

412 The aerosol/sheath ratio within the DMA also modulates the effect of multiple charges on  $\kappa_{app}$ . As the  
413 aerosol/sheath ratio increases, the transfer function broadens, allowing particles that are both larger and  
414 smaller than the selected diameter to exit the DMA. This in turn broadens the CCN activated fraction  
415 curve (Rose et al., 2008). The larger particles will activate as CCN at lower supersaturations than  
416 particles with the selected diameter, resulting in an increase in the activated fraction plateau due to  
417 multiple-charged particles and a further decrease in the determined  $SS_{crit}$ . Petters et al. 2007b showed  
418 that CCN activated fraction curves are significantly skewed by multiply-charged particles when the  
419 mode diameter of the aerosol population upstream of the DMA exceeds the critical diameter of the size-  
420 selected particles. In an example CCN activated fraction curve, Rose et al. 2008 demonstrated that a 1:6  
421 ratio of doubly-to-singly charged particles resulted in an underestimation of the critical activation  
422 diameter by 2%. Zhao-Ze and Liang, 2014 also showed that multiply-charged particles can introduce  
423 significant uncertainty into hygroscopicity calculations.

424

#### 425 **3.1.4 Additional artifacts resulting from DMA measurements**

426

427 Several additional factors that may impact experimental  $\kappa_{app}$  are beyond the scope of this study, but are  
428 worth mentioning as they represent additional potential sources of error in some cases. First, volatile  
429 aerosols may partially evaporate inside the DMA, resulting in a decrease in particle size exiting the  
430 DMA. DMA sizing error due to aerosol volatility (defined as the ratio of sampled diameter to the  
431 selected diameter) increases with volatility, though sizing error can be decreased by increasing the  
432 sheath flow rate in the DMA. Conversely, hygroscopic aerosols may grow inside the DMA, resulting in

433 larger particles existing the DMA. Operationally, errors in DMA sizing due to hygroscopic growth can  
434 be mitigated if aerosols entering the DMA inlet are in wet metastable states (higher aerosol RH at DMA  
435 inlet), and if DMA sheath flow rates are kept low (Khlystov, 2014).

436

437 Voltage shifts within the DMA (differences between the selected voltage and the actual voltage inside  
438 the DMA) can lead to discrepancies between selected and sampled particle diameters. Voltage shifts  
439 may result from a space-charge field generated by the motion of charges within the DMA. Particles  
440 charged by the bi-polar neutralizer will either be attracted towards or repelled away from the inner  
441 column of the DMA, depending on whether they are positively or negatively charged. This charge  
442 separation creates a space-charge field which shifts the actual voltage within the DMA from the selected  
443 voltage. The impact of the space-charge field on the midpoint and spread of the DMA transfer function  
444 increases as particle mobility increases (as particle size decreases), and as particle concentration  
445 increases (Alonso and Kousaka, 1996; Alonso et al., 2000; Alonso et al., 2001).

## 446 4. Artifacts derived from condensation particle counters

447

### 448 4.1 CPC operation at low concentration

449

450 The second instrument which must function accurately during CCN experiments is the condensation  
451 particle counter. CPC performance is characterized by the maximum counting efficiency (which may be  
452 influenced by the working fluid in the instrument) and the 50 %-cut-off diameter ( $d_{50}$ ), the particle  
453 diameter at which 50 % counting efficiency is observed, both of which can vary between commercially  
454 available models and even between individual CPCs (Heim et al., 2004). One study found that n-  
455 butanol CPCs (TSI, Inc. Models 3772, 3775, and 3776) exhibited smaller  $d_{50}$  for silver particles than  
456 sodium chloride ( $3.3 \text{ nm} \leq d_{50}^{Ag} \leq 7.8 \text{ nm}$  and  $4.1 \text{ nm} \leq d_{50}^{NaCl} \leq 14.7 \text{ nm}$ ), due to the more effective  
457 condensation of n-butanol on silver particles (Hermann et al., 2007).

458

459 Maximum counting efficiencies in that study varied from 88.9 % to 100.3 %. Another comparison of n-  
460 butanol CPCs (TSI Inc. Models 3010 and 3022, Grimm Tech. Inc. Model 5.403) found  $3.1 \text{ nm} \leq d_{50} \leq$   
461  $11.9 \text{ nm}$  for sodium chloride aerosols (Heim et al., 2004). In another study, the counting efficiencies  
462 observed in measurements of tungsten oxide particles by different instruments of the same model (TSI  
463 3025) varied from 88.9 % to 138.9 %, while  $d_{50}^{WO_x}$  varied from 3.2 nm to 11.0 nm (Hameri et al., 2002).

464

465 While some issues can cause undercounting at all concentrations, the additional issue of uncounted  
466 particles due to the arrival of more than one particle in the detector's field of view at any time arises  
467 only at higher concentrations. The cut-off between "low" and "high" concentration is not exact and  
468 varies between instruments. CPC undercounting issues which arise even at relatively low concentrations  
469 (which one would expect to encounter under standard experimental conditions) will be discussed in this

470 section. Concentration-dependent effects encountered at higher concentrations will be explored in Sect.  
471 4.2.

472  
473 Six counting efficiency curves were generated using sigmoidal distributions and the 50 % cut-off  
474 diameters and maximum counting efficiencies listed in Table 3. Chosen values represent  $d_{50}$  values and  
475 maximum counting efficiencies reported in the literature under relatively low concentrations of 1000-  
476 4000  $\text{cm}^{-3}$  (Hermann et al., 2007). The resulting sigmoidal distributions (Fig. 7a) were used to  
477 determine the counting efficiency of 25, 50, 100, and 200 nm particles.

478  
479 Next,  $\kappa_{app}$  was calculated from theoretical critical percent supersaturations for each chosen diameter. To  
480 do so, four sigmoid curves representing sodium chloride CCN activation (hereon referred to as  
481 “activation curves”) for 25, 50, 100, and 200 nm were generated. The  $\kappa$ -Köhler- $SS_{crit}$  of sodium  
482 chloride was used as the midpoint of each activation curve, and one-tenth of this value was used as the  
483 standard deviation (100 % CE, Fig. 7b-e). These values are consistent with the standard  
484 deviation/midpoint ratio observed from our instrument’s ammonium sulfate CCN calibration data.

485  
486 Activation curves were then generated for CPC Cases 1-6 by dividing the activated fraction for each dry  
487 particle diameter by the counting efficiency for that diameter.  $SS_{crit}$  was determined for each CPC case  
488 by finding the percent supersaturation at which activated fraction = 0.50. Results are summarized in  
489 Fig. 7f. Next, critical supersaturation was converted to saturation, and  $\kappa_{app,theory}$  was calculated for  
490 each diameter in each CPC Case using Eq. (4) (see Fig. 7g). As above,  $\kappa_{app}$  artifacts were calculated by  
491 finding the difference between these results and the literature value of  $\kappa_{app}$  for sodium chloride (see Fig.  
492 7h).

493

494 For the diameters studied, the effect of maximum counting efficiency on CPC concentration (and  
495 activated fraction) is greater than the effect of 50 %-cutoff diameter. However, neither characteristic  
496 resulted in large  $\kappa_{app}$  artifacts. The largest  $\kappa_{app}$  artifact observed at “low” concentrations was 0.035 for  
497 CPC Case 4, 2.4 % of the literature value for the apparent hygroscopicity factor for sodium chloride.

498 **4.2 CPC operation at high concentration**

499

500 Operation at high concentrations introduces an additional source of undercounting through particle  
501 coincidence at the CPC optical counter. For the TSI 3010 CPC, undercounting is observed is for particle  
502 concentrations above  $1 \times 10^4 \text{ cm}^{-3}$ . At  $5 \times 10^4 \text{ cm}^{-3}$ , the detector saturates and cannot detect higher  
503 concentrations. By comparison, the TSI 3025 is effective at counting higher particle concentrations, of  
504 up to  $2.5 \times 10^4 \text{ cm}^{-3}$  (Hameri et al., 2002; Sem, 2002).

505

506 To model undercounting due to particle coincidence, four CPC counting curves (Fig. 8a) were generated  
507 using the equations in Table 4. Case 7 represents a CPC where counting efficiency decreases with  
508 particle concentration, without reaching saturation. Cases 8-10 represent CPCs where saturation is  
509 reached at  $4 \times 10^4 \text{ cm}^{-3}$ ,  $2 \times 10^4 \text{ cm}^{-3}$ , and  $1 \times 10^4 \text{ cm}^{-3}$ , respectively. These saturation  
510 concentrations are of similar magnitude to those observed from TSI 3010 concentration data. It should  
511 be noted that the CPC concentration in Cases 7-10 levels off at the saturation concentration for each  
512 case.

513

514 In order to assess the importance of undercounting in CPC Cases 7-10, four theoretical aerosol  
515 distributions with a peak concentration at 50 nm were employed (Table 5, Fig. 8b). CPC Distribution 1  
516 represents a worst-case scenario of similar magnitude to the highest particle concentrations measured  
517 during a coastal nucleation event (Hameri et al., 2002; Sem, 2002), while CPC Distributions 2, 3, and 4  
518 are lower in concentration (due to the lack of undercounting in CPC Distributions 2, 3, and 4 as  
519 demonstrated in Figure 6b, the remaining analysis for CPC operation at high concentration considers  
520 only CPC Distribution 1.) CPC Cases 8-10 were applied to CPC Distribution 1 in order to determine the

521 concentration measured by the CPC for 25, 50, 100 and 200 nm aerosols. The counting efficiency was  
522 then calculated for each case and aerosol diameter in CPC Distribution 1.  
523  
524 Sigmoidal activated fraction curves were generated for 25, 50, 100 and 200 nm sodium chloride  
525 aerosols. As in the low concentration cases, the midpoint of each 100 % CE curve was chosen to be  
526 equal to the  $\kappa$ -Köhler-derived  $SS_{crit}$  of sodium chloride at each dry diameter, and the standard deviation  
527 of each curve is equal to one-tenth of the  $SS_{crit}$ . These activated fraction curves were adjusted using the  
528 counting efficiencies calculated in the previous step. In cases where the activated fraction has increased  
529 due to undercounting by the CPC, the theoretical sigmoidal curve shifts to the left relative to the 100 %  
530 CE case (Fig. 8c-f). Thus, undercounting by the CPC effectively increases the reported activated  
531 fraction. As before,  $SS_{crit}$  was determined from each of these curves, and  $\kappa_{app,theory}$  was subsequently  
532 calculated using Eq. (4) (Fig. 8g-h).  
533  
534  $\kappa_{app,theory}$  fell over a much wider range for 25, 50, and 100 nm particles (1.30-1.56, 1.32-1.70, and  
535 1.30-1.55, respectively) than for 200 nm particles (1.28-1.29) due to the lower concentration of 200 nm  
536 particles in the chosen aerosol distribution, which resulted in a higher counting efficiency for these  
537 aerosols. In comparison, the largest range in  $\kappa_{app,theory}$  was observed for 50 nm aerosols, the peak  
538 diameter in this aerosol distribution.  
539  
540 A wider range in  $\kappa_{app,theory}$  was observed for the high-concentration CPC Cases (7-10) compared to the  
541 low-concentration CPC Cases (1-6). The lowest counting efficiency observed across the low-  
542 concentration cases was 89.9 % for 25 nm aerosol in Case 4, while the lowest counting efficiency  
543 observed in the high-concentration cases was 18.0 % for 50 nm aerosol in Case 10.  
544



545 Artifacts in the apparent hygroscopicity parameter are shown in Fig. 8i.  $\kappa_{app}$  artifacts were the greatest  
546 for a CPC that becomes saturated at 20,000 particles/cm<sup>3</sup> ( $0.0131 \leq \kappa_{app} \leq 0.4206$ ). The lower the  
547 concentration at which a CPC becomes saturated, the more quickly its counting efficiency will drop as  
548 concentration increases, resulting in increased activated fraction and increased apparent hygroscopicity.  
549 The magnitude of artifacts due to CPC undercounting depends on the saturation concentration of the  
550 CPC and the distribution of the aerosol population being studied.

551 **5. Artifacts derived from cloud condensation nuclei instruments**

552

553 Finally, the third instrument whose performance accuracy contributes to the overall certainty in CCN  
554 assessment in the CCN instrument itself. Several instruments have been implemented for measuring  
555 CCN concentrations over the last few decades. Older models include the Continuous Flow Parallel Plate  
556 Diffusion Chamber (Sinnarwalla, 1973) and the Hudson CCN spectrometer (Hudson, 1989) which both  
557 employ an applied temperature gradient perpendicular to the aerosol flow. Newer models, such as the  
558 widely-used Droplet Measurement Technology Cloud Condensation Nuclei Counter (DMT CCN-100),  
559 operate with a streamwise temperature gradient and continuous, laminar flow (Lance et al., 2006). The  
560 total flow through the DMT CCN-100 is 0.20-0.90 L min<sup>-1</sup>, though the instrument is typically operated  
561 with a total flow of 0.50 L min<sup>-1</sup>. The aerosol/sheath ratio in the DMT CCN-100 is set by the user, and a  
562 ratio of 1:10 is commonly chosen. The following analysis considers the DMT CCN-100. According to  
563 the CCN-100 manual, the counting efficiency for this CCN instrument depends on concentration and  
564 supersaturation (Fig. 9a). The counting efficiency decreases rapidly with concentration at < 0.2 % SS  
565 due to rapid water vapor depletion at these low supersaturations, and falls off more slowly for > 0.2 %  
566 SS (DMT CCN-100 manual).

567

568 The counting efficiency of the DMT CCN-100 was tested for four lognormal aerosol distributions with  
569 peak concentrations at 50 nm and varying total concentrations (Table 5, Fig. 9b). Note that CCN Cases  
570 1-4 are identical to the aerosol distributions CPC Distributions 1-4 used for the high-concentration CPC  
571 cases.

572

573 The counting efficiencies for each case were applied to theoretical sodium chloride sigmoidal activated  
574 fraction curves to produce normalized activated fraction curves (Fig. 9c-f). As above, the midpoint is

575 set to the  $SS_{crit}$  of sodium chloride at each dry diameter, and the standard deviation is assumed to be  
576 one-tenth of  $SS_{crit}$ . CCN undercounting effectively decreases activated fraction, therefore shifting the  
577 activated fraction curve downwards and towards higher percent supersaturations. The opposite effect is  
578 observed when CPC undercounting occurs. Critical supersaturation was determined for each CCN case,  
579 as above (Fig. 9g). Values of  $SS_{crit}$  were then converted to saturation, and  $\kappa_{app,theory}$  was calculated  
580 using Eq. (4) (Fig. 9h).

581

582 Significant deviations from  $\kappa$ -Köhler theory were only observed in CCN Case 1, with total aerosol  
583 concentration  $5 \times 10^6$  particles/cm<sup>3</sup> (Fig. 9g-i). The largest deviation for CCN Case 1 was observed in  
584 100 nm particles ( $\kappa_{app,artifact} = -0.57$ ), due to the higher concentration of 100 nm particles compared  
585 to 25 and 200 nm particles, and the lower percent supersaturation necessary for activation. The largest  
586 artifacts across CCN Cases 2 and 3 were also observed for 100 nm particles, though no artifacts were  
587 observed for any particle diameter in CCN Case 4 due to the much lower concentrations.

588

589 Sodium chloride is very hygroscopic. It should be noted that aerosols consisting of less hygroscopic  
590 compounds will activate at higher percent supersaturations (> 0.2 % SS regime) which will lead to  
591 smaller  $\kappa_{app}$  artifacts when the same aerosol distribution and total aerosol concentration is considered.  
592 If a mixture was considered (for example, sodium chloride with a non-hygroscopic species such as soot)  
593 the results may also be different. The shape of the aerosol distribution must also be taken into account.  
594 A distribution with a narrower peak than the one generated for this analysis would be at risk for larger  
595  $\kappa_{app}$  artifacts for any total aerosol concentration, and these artifacts would be greater at the peak  
596 diameter, while a broader distribution would result in less variation in  $\kappa_{app}$  artifacts for each particle  
597 diameter.

## 598 6. Counting statistics in CCN and CPC measurements

599

600 Though it is beyond the scope of this analysis, it should be mentioned that sampling at very low particle  
601 concentrations ( $< 200 \text{ cm}^{-3}$  total particle concentration) can introduce additional error into CCN and  
602 CPC measurements. This error can be mitigated by increasing scan times (Moore et al., 2010). For  
603 example, Moore et al., 2010 averaged CCN and particle concentrations over 5-second intervals for  
604 monodisperse particle concentrations  $< 10 \text{ cm}^{-3}$ , and increased averaging time to 20-second intervals  
605 when the monodisperse particle concentration reached  $< 6 \text{ cm}^{-3}$ .

606

## 607 7. Discussion

608

609 A comparison of the major instrument sources of error in CCN-derived  $\kappa_{app}$  is shown in Fig. 10. In  
610 addition, the best and worst case combination of errors, determined by additive error propagation, are  
611 also shown. DMA Case 4, CPC Case 4, CPC Case 10, and CCN Case 1 represent the operating  
612 conditions that resulted in the largest  $\kappa_{app}$  artifacts in this study. In DMA Case 4, the aerosol/sheath  
613 ratio of 0.30 resulted in a broadened aerosol distribution downstream of the DMA. Compared to DMA  
614 Case 1, where  $Q_a/Q_{sh} = 0.10$ , the downstream diameter range in DMA Case 4 was 300 % higher for 25  
615 nm particles, resulting in a spread of 20-36 nm. Similarly, the diameter ranges for 50, 100, and 200 nm  
616 diameter were 220 %, 230 %, and 220 % wider than in Case 1, respectively. Compared to the most ideal  
617 DMA case presented in this study (DMA Case 2), where  $Q_a/Q_{sh} = 0.05$ , the downstream diameter  
618 range in DMA Case 4 was 700 % higher for 25 nm particles; the diameter ranges for 50, 100, and 200  
619 nm diameter were 540 %, 560 %, and 520 % wider than in Case 2, respectively. The results  
620 demonstrate that limiting  $Q_a/Q_{sh}$  to  $\leq 0.10$  will result in a narrow particle size distribution downstream  
621 of the DMA. Other studies have recommended employing DMA sample/sheath ratios of 0.2 (Petters et

622 al., 2007; Carrico et al., 2008; Moore et al., 2010) or 0.1 (Moore et al., 2010; Zhao-Ze and Liang, 2014)  
623 in order to minimize measurement aerosols due to transfer function broadening.

624

625 The effects of multiply-charged particles on  $\kappa_{app}$  calculations were also quantified, as shown in Fig. 10.  
626 Small, positive  $\kappa_{app}$  artifacts (1 – 3 % of  $\kappa_{app}^{NaCl}$ ) were observed when particles with +2 and +3 charges  
627 were not accounted for. This analysis considered a theoretical aerosol distribution in which most of the  
628 particles measure less than 100 nm in diameter. Actual aerosol distributions vary temporally and  
629 spatially, and often include accumulation and coarse modes that would result in larger  $\kappa_{app}$  artifacts.

630

631 CPC Case 4 represents  $\kappa_{app}$  artifacts (0.031-0.035) due to undercounting that arises from poor  
632 maximum CPC counting efficiency (90 %), which may be observed when using butanol as a working  
633 fluid while measuring the concentration of inorganic aerosols. In contrast,  $\kappa_{app}$  artifacts are negligible  
634 ( $< 0.10$  % of  $\kappa_{app}^{NaCl}$ ) in CPC Case 3, where maximum counting efficiency = 100 %. CPC Cases 8 and 10  
635 (applied to the highest-concentration case, CPC Distribution 1) represent undercounting at high  
636 concentration with CPCs where saturation is observed at  $4 \times 10^4 \text{ cm}^{-3}$  and  $1 \times 10^4 \text{ cm}^{-3}$ , respectively.  
637 Counting efficiency drops off more rapidly with concentration in the latter case, resulting in  $\kappa_{app}$   
638 artifacts that are highest at the peak of the aerosol distribution (0.1190 and 0.4206 for 50 nm aerosols in  
639 CPC Cases 8 and 10, respectively). It should be noted that undercounting was only observed for one of  
640 the four upstream distributions studied, CPC Distribution 1. No undercounting was observed when CPC  
641 Cases 7-10 were applied to CPC Distributions 2-4.

642

643 CCN Case 1 represents CCN undercounting at high concentration (total aerosol concentration =  $5 \times$   
644  $10^6 \text{ cm}^{-3}$ ). CCN undercounting is greatest for low supersaturation ( $< 0.2$  %) and high concentration,

645 resulting in the lowest counting efficiency and highest  $\kappa_{app}$  artifacts (- 0.57) for 100 nm aerosols in  
646 CCN Case 1. The largest CCN-derived  $\kappa_{app}$  artifact observed outside of CCN Case 1 was - 0.01 for  
647 100 nm aerosols in CCN Case 2.

648

649 The combined artifacts for the cases where the highest artifacts were observed (DMA Case 4, multiple  
650 particle charging, CPC Case 4, CPC Case 10, CCN Case 1) are 0.24, 0.21, 0.23, and 0.15 for 25, 50,  
651 100, and 200 nm particles respectively, as shown in Fig. 10. The combined artifacts for the lowest-  
652 artifact cases (DMA Case 2, CPC Case 3, and CCN Case 4) are < 0.008 except for all four particle  
653 diameters.

654

655

656 **Conclusions**

657

658 The sensitivity of weather and climate models to accuracy in CCN activation predictions has been  
659 demonstrated in other works. Possible sources of apparent hygroscopicity artifacts calculated from CCN  
660 measurements have been presented in this study. This analysis has focused on sodium chloride and  
661 ammonium sulfate aerosols, but it can be extended to other aerosol populations, including mixtures and  
662 field samples.

663

664 The greatest combined artifacts ( $0.15 < \kappa_{app,artifact} < 0.24$ , NaCl) occurred as a result of the  
665 combined issues of the highest DMA aerosol/sheath ratio, uncorrected multiple particle charging, and  
666 undercounting by both CPC and CCN instrument. The lowest combined artifacts ( $0.0021 <$   
667  $\kappa_{app,artifact} < 0.0074$ , NaCl) occurred as a result of ideal operating conditions: lowest DMA/sheath  
668 ratio, corrected multiple particle charging, and little to no undercounting.

669

670 The largest single-instrument artifacts ( $-0.57 < \kappa_{app,artifact} < 0.42$  for sodium chloride) in this study  
671 arise from undercounting by either the CPC or CCN counter at high concentration. This problem occurs  
672 during attempts to measure aerosol concentrations of  $\sim 10^4 \text{ cm}^{-3}$  which is much higher than the  
673 recommended concentration ranges for either instrument, (CPC Cases 7-10 and CCN Case 4).

674 Corrective action should be taken to dilute aerosol samples in order to avoid undercounting. It should be  
675 noted that these artifacts are for individual instruments and do not take combined operation of the CPC  
676 and CCN into account; when both instruments undercount, artifacts in  $\kappa_{app,artifact}$  are reduced.

677

678 Smaller single-instrument artifacts ( $\kappa_{app,artifact} < 0.04$ ) were observed for the CPC cases where 50 %-  
679 cut-off diameter and maximum counting efficiency were varied. Given the chosen particle diameters

680 (25, 50, 100, 200 nm),  $\kappa_{app}$  artifacts due to  $d_{50}$  were minimal. The largest  $\kappa_{app}$  artifacts for a CPC  
681 counting at low concentration (0.031-0.035) were observed where the maximum counting efficiency was  
682 equal 0.90. This may represent a compositional mismatch between n-butanol as the working fluid and  
683 sodium chloride as the aerosol, due to the poor solubility of the latter in the former. Individual n-butanol  
684 CPCs may exhibit higher maximum counting efficiencies for sodium chloride.

685

686 Uncertainty arising from the DMA depended greatly on the chosen aerosol and sheath settings. One set  
687 of DMA cases (Cases 2-4) examined the effect of aerosol/sheath ratio. By decreasing this ratio, a  
688 narrower near-monodisperse flow can be produced, which increases the accuracy of calculated  $\kappa_{app}$ .

689 The  $\kappa_{app}$  artifacts for an aerosol/sheath ratio of 0.10 were 0.65 % of  $\kappa_{literature}$  for 25 nm sodium  
690 chloride aerosols, 0.31 % for 50 nm, -0.17 % for 100 nm, and -1.2 % for 200 nm.

691

692 The second set of DMA cases (5-7) were designed to evaluate the effects of holding the sheath flow  
693 constant while varying the excess air flow by -2 %, +2 %, and +5 %. These resulted in shifts of  $\leq 2$  nm  
694 for 25 nm and 50 nm particles,  $\leq 4$  nm for 100 nm particles, and  $\leq 7$  nm for 200 nm particles. The  
695 downstream aerosol distribution was shifted towards larger particle diameters when sheath flow  
696 exceeded excess flow, and towards smaller particle diameter when sheath flow was less than excess  
697 flow. When taking field measurements, the composition of the sample may vary with particle diameter,  
698 thereby introducing another source of error from a broader DMA distribution.

699

700 By extension, the issue of uncertain sizing by the DMA leads to added uncertainties in the CCN  
701 instrument calibrations which are strongly dependent on the chosen aerosol to sheath ration within the  
702 DMA. We recommend conducting all CCN calibrations with DMA aerosol to sheath ratio of 1:10 or  
703 1:20 which will reduce kappa uncertainties to less than 1% for all dry sizes (25 to 200 nm).



704

705 Overall, under optimal operating conditions, where the DMA aerosol/sheath ratio is 0.10 and  
706 excess/sheath ratio is 1.0, and in the absence of undercounting by the CPC or CCN, uncertainties in  $\kappa_{app}$   
707 are less than  $\pm 1.2\%$  for 25 to 200 nm particles. During sampling, when the DMA sample/sheath ratio is  
708 reduced to 0.05,  $\kappa_{app}$  uncertainties decrease to  $\pm 0.58\%$ . Additionally, errors in activated fraction (and  
709 therefore  $\kappa_{app}$ ) resulting from the bipolar charge distribution can be corrected by determining the  
710 fraction of particles with multiple charges.

711

712 In this study, apparent hygroscopicity parameter artifacts were calculated for two pure, inorganic species  
713 in this study. This analysis could be used to estimate  $\kappa_{app}$  artifacts for ambient aerosol populations,  
714 which may result in a better understanding of the “real” differences between these populations. As  
715 discussed in the introduction, Collins et al. 2016 aggregated  $\kappa_{app}$  from several mesocosm and field  
716 studies for 30-100 nm sea spray aerosol ( $0.4 < \kappa_{app}^{SSA} < 1.3$ ). The wide range of  $\kappa_{app}$  in these studies  
717 may be attributed to differences in composition, experimental artifacts, or a combination of the two.  
718 Quantification of experimental artifacts would facilitate interpretation of  $\kappa_{app}$  in aerosol populations and  
719 constrain the importance of composition in CCN activation. There has been a recent proliferation of  
720 CCN data availability from multiple researchers and multiple experimental setups. To maximize the  
721 utility of these studies and to compare cloud-activating properties of various ambient aerosol masses, it  
722 is essential that artifacts are considered in both CCN data collection and in reporting of the data.

723 **Supplement Link**

724 Will be included by Copernicus

725

726 **Author Contribution**

727 Sarah D. Brooks provided the conceptual framework and contributed to the writing of the manuscript.

728 Jessica A. Mirrieles performed the analysis and lead the writing of the manuscript.

729

730 **Competing Interests**

731 The authors declare that they have no conflict of interest.

732

733 **Disclaimer**

734 Will be included by Copernicus

735

736 **Acknowledgements**

737 This project was supported by the National Science Foundation of the United States (Award

738 #15398810). In addition, Mirrieles thanks Texas A&M University for support through Institute for and

739 Advanced Studies HEEP PhD Fellowship and a Lechner Scholarship.

740 **References**

- 741 Alonso, M., and Kousaka, Y.: Mobility shift in the differential mobility analyzer due to Brownian  
742 diffusion and space-charge effects, *J. Aerosol. Sci.*, 27, 1201-1225, 10.1016/0021-8502(96)00052-3,  
743 1996.  
744
- 745 Alonso, M., Alguacil, F. J., and Kousaka, Y.: Space-charge effects in the differential mobility analyzer,  
746 *J. Aerosol. Sci.*, 31, 233-247, 10.1016/s0021-8502(99)00051-8, 2000.  
747
- 748 Alonso, M., Alguacil, F. J., Watanabe, Y., Nomura, T., and Kousaka, Y.: Experimental evidence of  
749 DMA voltage shift due to space-charge, *Aerosol Sci. Technol.*, 35, 921-923, 10.1080/02786820126855,  
750 2001.  
751
- 752 Asa-Awuku, A., Nenes, A., Gao, S., Flagan, R. C., and Seinfeld, J. H.: Water-soluble SOA from Alkene  
753 ozonolysis: composition and droplet activation kinetics inferences from analysis of CCN activity,  
754 *Atmos. Chem. Phys.*, 10, 1585-1597, 10.5194/acp-10-1585-2010, 2010.  
755
- 756 Andreae, M. O., and D. Rosenfeld. 2008. "Aerosol-cloud-precipitation interactions. Part 1. The nature  
757 and sources of cloud-active aerosols." *Earth-Science Reviews* 89 (1-2):13-41. doi:  
758 10.1016/j.earscirev.2008.03.001.  
759
- 760 Barmounis, K., Maisser, A., Schmidt-Ott, A., and Biskos, G.: Lightweight differential mobility  
761 analyzers: Toward new and inexpensive manufacturing methods, *Aerosol Sci. Technol.*, 50, 4,  
762 10.1080/02786826.2015.1130216, 2016.  
763
- 764 Betancourt, R. M., Nenes, A., and Liu, X. H.: Relative Contributions of Aerosol Properties to Cloud  
765 Droplet Number: Adjoint Sensitivity Approach in a GCM, in: *AIP Conference Proceedings*, 19th  
766 International Conference on Nucleation and Atmospheric Aerosols (ICNAA), Colorado State Univ, Ctr  
767 Arts, Fort Collins, CO, 2013, WOS:000319766400170, 679-682, 2013.  
768
- 769 Betancourt, R. M., and Nenes, A.: Understanding the contributions of aerosol properties and  
770 parameterization discrepancies to droplet number variability in a global climate model, *Atmos. Chem.*  
771 *Phys.*, 14, 4809-4826, 10.5194/acp-14-4809-2014, 2014.  
772
- 773 Bougiatioti, A., Fountoukis, C., Kalivitis, N., Pandis, S. N., Nenes, A., and Mihalopoulos, N.: Cloud  
774 condensation nuclei measurements in the marine boundary layer of the eastern Mediterranean: CCN  
775 closure and droplet growth kinetics, *Atmos. Chem. Phys.*, 9, 7053-7066, 10.5194/acp-9-7053-2009,  
776 2009.  
777
- 778 Brooks, S. D., and Thornton, D. C. O.: Marine Aerosols and Clouds, in: *Annual Review of Marine*  
779 *Sciences*, Vol 10, edited by: Carlson, C. A., and Giovannoni, S. J., *Annual Review of Marine Science*,  
780 289-313, 2018.  
781
- 782 Carrico, C. M., Petters, M. D., Kreidenweis, S. M., Collett, J. L., Engling, G., and Malm, W. C.: Aerosol  
783 hygroscopicity and cloud droplet activation of extracts of filters from biomass burning experiments, *J.*  
784 *Geophys. Res.-Atmos.*, 113, 9, 10.1029/2007jd009274, 2008.  
785

786 Carslaw, K. S., Lee, L. A., Reddington, C. L., Pringle, K. J., Rap, A., Forster, P. M., Mann, G. W.,  
787 Spracklen, D. V., Woodhouse, M. T., Regayre, L. A., and Pierce, J. R.: Large contribution of natural  
788 aerosols to uncertainty in indirect forcing, *Nature*, 503, 67-+, 10.1038/nature12674, 2013.  
789  
790 Chang, D. Y., Lelieveld, J., Tost, H., Steil, B., Pozzer, A., and Yoon, J.: Aerosol physicochemical  
791 effects on CCN activation simulated with the chemistry-climate model EMAC, *Atmospheric*  
792 *Environment*, 162, 127-140, 10.1016/j.atmosenv.2017.03.036, 2017.  
793  
794 Clegg, S. L., Brimblecombe, P., and Wexler, A. S.: Thermodynamic model of the system  $H^+-NH_4^+$ -  
795  $SO_4^{2-}-NO_3^- -H_2O$  at tropospheric temperatures, *J. Phys. Chem. A*, 102, 2137-2154, 10.1021/jp973042r,  
796 1998.  
797  
798 Collins, D. B., Bertram, T. H., Sultana, C. M., Lee, C., Axson, J. L., and Prather, K. A.: Phytoplankton  
799 blooms weakly influence the cloud forming ability of sea spray aerosol, *Geophys. Res. Lett.*, 43, 9975-  
800 9983, 10.1002/2016gl069922, 2016.  
801  
802 Crosbie, E., Youn, J. S., Balch, B., Wonaschutz, A., Shingler, T., Wang, Z., Conant, W. C., Betterton, E.  
803 A., and Sorooshian, A.: On the competition among aerosol number, size and composition in predicting  
804 CCN variability: a multi-annual field study in an urbanized desert, *Atmos. Chem. Phys.*, 15, 6943-6958,  
805 10.5194/acp-15-6943-2015, 2015.  
806  
807 DeCarlo, P. F., Slowik, J. G., Worsnop, D. R., Davidovits, P., and Jimenez, J. L.: Particle morphology  
808 and density characterization by combined mobility and aerodynamic diameter measurements. Part 1:  
809 Theory, *Aerosol Sci. Technol.*, 38, 1185-1205, 10.1080/027868290903907, 2004.  
810  
811 Duan, J. Y., Tao, J., Wu, Y. F., Cheng, T. T., Zhang, R. J., Wang, Y. Y., Zhu, H. Y., Xie, X., Liu, Y. H.,  
812 Li, X., Kong, L. D., Li, M., and He, Q. S.: Comparison of aerosol and cloud condensation nuclei  
813 between wet and dry seasons in Guangzhou, southern China, *Sci. Total Environ.*, 607, 11-22,  
814 10.1016/j.scitotenv.2017.06.246, 2017.  
815  
816 Fitzgerald, J. W.: Approximation formulas for equilibrium size of an aerosol particle as a function of its  
817 dry size and composition and relative humidity, *Journal of Applied Meteorology*, 14, 1044-1049,  
818 10.1175/1520-0450(1975)014<1044:afftes>2.0.co;2, 1975.  
819  
820 Fitzgerald, J. W., Hoppel, W. A., and Vietti, M. A.: The size and scattering coefficient of urban aerosol  
821 particles at Washington, DC as a function of relative humidity, *Journal of the Atmospheric Sciences*, 39,  
822 1838-1852, 10.1175/1520-0469(1982)039<1838:tsasco>2.0.co;2, 1982.  
823  
824 Hameri, K., O'Dowd, C. D., and Hoell, C.: Evaluating measurements of new particle concentrations,  
825 source rates, and spatial scales during coastal nucleation events using condensation particle counters, *J.*  
826 *Geophys. Res.-Atmos.*, 107, 11, 10.1029/2001jd000411, 2002.  
827  
828 Hartz, K. E. H., Tischuk, J. E., Chan, M. N., Chan, C. K., Donahue, N. M., and Pandis, S. N.: Cloud  
829 condensation nuclei activation of limited solubility organic aerosol, *Atmospheric Environment*, 40, 605-  
830 617, 10.1016/j.atmosenv.2005.09.076, 2006.  
831  
832 Heim, M., Kasper, G., Reischl, G., and Gerhart, C.: Performance of a New Commercial Electrical  
833 Mobility Spectrometer, *Aerosol Sci. Technol.*, 38, 3-14, 10.1080/02786820490519252, 2004.

834  
835 Hermann, M., Wehner, B., Bischof, O., Han, H. S., Krinke, T., Liu, W., Zerrath, A., and Wiedensohler,  
836 A.: Particle counting efficiencies of new TSI condensation particle counters, *J. Aerosol. Sci.*, 38, 674-  
837 682, 10.1016/j.jaerosci.2007.05.001, 2007.  
838  
839 Hoppel, W. A., and Frick, G. M.: The nonequilibrium character of the aerosol charge distributions  
840 produced by neutralizers, *Aerosol Sci. Technol.*, 12, 471-496, 10.1080/02786829008959363, 1990.  
841  
842 Hudson, J. G.: An Instantaneous CCN Spectrometer, *J. Atmos. Ocean. Technol.*, 6, 1055-1065,  
843 10.1175/1520-0426(1989)006<1055:aics>2.0.co;2, 1989.  
844  
845 Hudson, J. G., and Xie, Y. H.: Cloud condensation nuclei measurements in the high troposphere and in  
846 jet aircraft exhaust, *Geophys. Res. Lett.*, 25, 1395-1398, 10.1029/97gl03705, 1998.  
847  
848 IPCC, 2013: Summary for Policymakers, Intergovernmental Panel on Climate Change, Cambridge  
849 University Press, 14, 2013.  
850  
851 Jennings, S. G., Geever, M., and Oconnor, T. C.: Surface CCN measurements at Mace Head, on the west  
852 coast of Ireland, *Nucleation and Atmospheric Aerosols 1996*, 800-803, 10.1016/b978-008042030-  
853 1/50193-1, 1996.  
854  
855 Jokinen, V., and Makela, J. M.: Closed-loop arrangement with critical orifice for DMA sheath excess  
856 flow system, *J. Aerosol. Sci.*, 28, 643-648, 10.1016/s0021-8502(96)00457-0, 1997.  
857  
858 Karydis, V. A., Capps, S. L., Russell, A. G., and Nenes, A.: Adjoint sensitivity of global cloud droplet  
859 number to aerosol and dynamical parameters, *Atmos. Chem. Phys.*, 12, 9041-9055, 10.5194/acp-12-  
860 9041-2012, 2012.  
861  
862 Kawecki, S., and Steiner, A. L.: The Influence of Aerosol Hygroscopicity on Precipitation Intensity  
863 During a Mesoscale Convective Event, *J. Geophys. Res.-Atmos.*, 123, 424-442, 10.1002/2017jd026535,  
864 2018.  
865  
866 Keefe, D., Nolan, P. J., and Rich, T. A.: Charge Equilibrium in Aerosols According to the Boltzmann  
867 Law, *Proceedings of the Royal Irish Academy. Section A: Mathematical and Physical Sciences*, 60, 27-  
868 45, 1959.  
869  
870 Khlystov, A.: Effect of Aerosol Volatility on the Sizing Accuracy of Differential Mobility Analyzers,  
871 *Aerosol Sci. Technol.*, 48, 604-619, 10.1080/02786826.2014.899681, 2014.  
872  
873 Knutson, E. O., and Whitby, K. T.: Aerosol classification by electric mobility: apparatus, theory, and  
874 applications, *J. Aerosol. Sci.*, 6, 443-451, [https://doi.org/10.1016/0021-8502\(75\)90060-9](https://doi.org/10.1016/0021-8502(75)90060-9), 1975.  
875  
876 Koehler, K. A., Kreidenweis, S. M., DeMott, P. J., Prenni, A. J., Carrico, C. M., Ervens, B., and  
877 Feingold, G.: Water activity and activation diameters from hygroscopicity data - Part II: Application to  
878 organic species, *Atmos. Chem. Phys.*, 6, 795-809, 10.5194/acp-6-795-2006, 2006.  
879

880 Kreidenweis, S. M., Koehler, K., DeMott, P. J., Prenni, A. J., Carrico, C., and Ervens, B.: Water activity  
881 and activation diameters from hygroscopicity data - Part I: Theory and application to inorganic salts,  
882 *Atmos. Chem. Phys.*, 5, 1357-1370, 10.5194/acp-5-1357-2005, 2005.  
883  
884 Kumar, P. P., Broekhuizen, K., and Abbatt, J. P. D.: Organic acids as cloud condensation nuclei:  
885 Laboratory studies of highly soluble and insoluble species, *Atmos. Chem. Phys.*, 3, 509-520, 2003.  
886 Lance, S., Medina, J., Smith, J. N., and Nenes, A.: Mapping the operation of the DMT Continuous Flow  
887 CCN counter, *Aerosol Sci. Technol.*, 40, 242-254, 10.1080/02786820500543290, 2006.  
888  
889 Leng, C. P., Cheng, T. T., Chen, J. M., Zhang, R. J., Tao, J., Huang, G. H., Zha, S. P., Zhang, M. G.,  
890 Fang, W., Li, X., and Li, L.: Measurements of surface cloud condensation nuclei and aerosol activity in  
891 downtown Shanghai, *Atmospheric Environment*, 69, 354-361, 10.1016/j.atmosenv.2012.12.021, 2013.  
892  
893 Liu, X. H., and Wang, J. A.: How important is organic aerosol hygroscopicity to aerosol indirect  
894 forcing?, *Environ. Res. Lett.*, 5, 10, 10.1088/1748-9326/5/4/044010, 2010.  
895  
896 Mamakos, A., Ntziachristos, L., and Sarnaras, Z.: Diffusion broadening of DMA transfer functions.  
897 Numerical validation of Stolzenburg model, *J. Aerosol. Sci.*, 38, 747-763,  
898 10.1016/j.jaerosci.2007.05.004, 2007.  
899  
900 Maricq, M. M.: Bipolar diffusion charging of soot aggregates, *Aerosol Sci. Technol.*, 42, 247-254,  
901 10.1080/02786820801958775, 2008.  
902  
903 Mei, F., Fu, H. J., and Chen, D. R.: A cost-effective differential mobility analyzer (cDMA) for multiple  
904 DMA column applications, *J. Aerosol. Sci.*, 42, 462-473, 10.1016/j.jaerosci.2011.04.001, 2011.  
905  
906 Mochida, M., Kuwata, M., Miyakawa, T., Takegawa, N., Kawamura, K., and Kondo, Y.: Relationship  
907 between hygroscopicity and cloud condensation nuclei activity for urban aerosols in Tokyo, *J. Geophys.*  
908 *Res.-Atmos.*, 111, 20, 10.1029/2005jd006980, 2006.  
909  
910 Modini, R. L., Frossard, A. A., Ahlm, L., Russell, L. M., Corrigan, C. E., Roberts, G. C., Hawkins, L.  
911 N., Schroder, J. C., Bertram, A. K., Zhao, R., Lee, A. K. Y., Abbatt, J. P. D., Lin, J., Nenes, A., Wang,  
912 Z., Wonaschutz, A., Sorooshian, A., Noone, K. J., Jonsson, H., Seinfeld, J. H., Toom-Sauntry, D.,  
913 Macdonald, A. M., and Leitch, W. R.: Primary marine aerosol-cloud interactions off the coast of  
914 California, *J. Geophys. Res.-Atmos.*, 120, 4282-4303, 10.1002/2014jd022963, 2015.  
915  
916 Moore, R. H., Nenes, A., and Medina, J.: Scanning Mobility CCN Analysis-A Method for Fast  
917 Measurements of Size-Resolved CCN Distributions and Activation Kinetics, *Aerosol Sci. Technol.*, 44,  
918 861-871, 10.1080/02786826.2010.498715, 2010.  
919  
920 Moore, R. H., Bahreini, R., Brock, C. A., Froyd, K. D., Cozic, J., Holloway, J. S., Middlebrook, A. M.,  
921 Murphy, D. M., and Nenes, A.: Hygroscopicity and composition of Alaskan Arctic CCN during April  
922 2008, *Atmos. Chem. Phys.*, 11, 11807-11825, 10.5194/acp-11-11807-2011, 2011.  
923  
924 Moore, R. H., Cerully, K., Bahreini, R., Brock, C. A., Middlebrook, A. M., and Nenes, A.:  
925 Hygroscopicity and composition of California CCN during summer 2010, *J. Geophys. Res.-Atmos.*,  
926 117, 14, 10.1029/2011jd017352, 2012.  
927

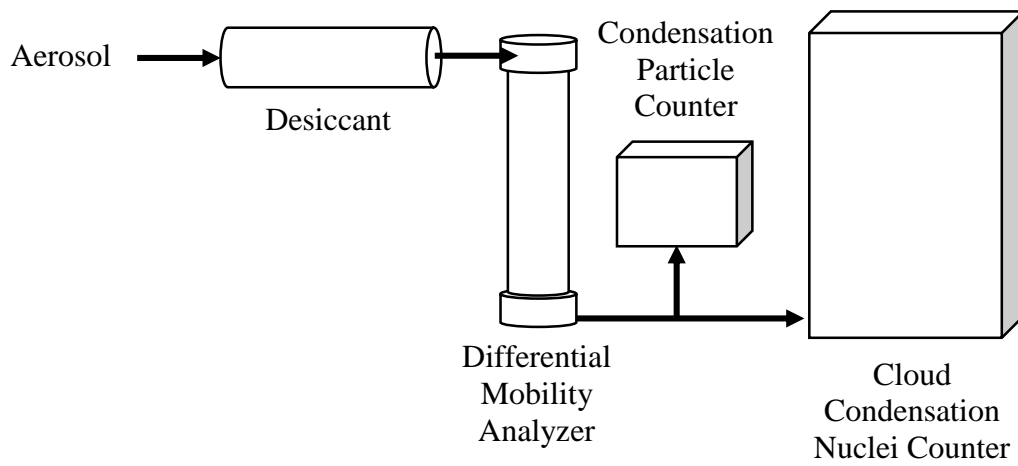
928 Moore, R. H., Raatikainen, T., Langridge, J. M., Bahreini, R., Brock, C. A., Holloway, J. S., Lack, D.  
929 A., Middlebrook, A. M., Perring, A. E., Schwarz, J. P., Spackman, J. R., and Nenes, A.: CCN Spectra,  
930 Hygroscopicity, and Droplet Activation Kinetics of Secondary Organic Aerosol Resulting from the 2010  
931 Deepwater Horizon Oil Spill, *Environ. Sci. Technol.*, 46, 3093-3100, 10.1021/eS303362w, 2012.  
932  
933 Ovadnevaite, J., Ceburnis, D., Martucci, G., Bialek, J., Monahan, C., Rinaldi, M., Facchini, M. C.,  
934 Berresheim, H., Worsnop, D. R., and O'Dowd, C.: Primary marine organic aerosol: A dichotomy of low  
935 hygroscopicity and high CCN activity, *Geophys. Res. Lett.*, 38, 5, 10.1029/2011gl048869, 2011.  
936  
937 Petters, M. D., and Kreidenweis, S. M.: A single parameter representation of hygroscopic growth and  
938 cloud condensation nucleus activity, *Atmos. Chem. Phys.*, 7, 1961-1971, 10.5194/acp-7-1961-2007,  
939 2007.  
940  
941 Petters, M. D., Prenni, A. J., Kreidenweis, S. M., and DeMott, P. J.: On measuring the critical diameter  
942 of cloud condensation nuclei using mobility selected aerosol, *Aerosol Sci. Technol.*, 41, 907-913,  
943 10.1080/02786820701557214, 2007.  
944  
945 Petters, M. D., and Kreidenweis, S. M.: A single parameter representation of hygroscopic growth and  
946 cloud condensation nucleus activity - Part 3: Including surfactant partitioning, *Atmos. Chem. Phys.*, 13,  
947 1081-1091, 10.5194/acp-13-1081-2013, 2013.  
948  
949 Rogers, R. R., and Yau, M. K.: in: *A Short Course In Cloud Physics*, Third ed., edited by: Haar, D. T.,  
950 Elsevier Science Inc., Tarrytown, New York, USA, 87-89, 1989.  
951  
952 Rose, D., Gunthe, S. S., Mikhailov, E., Frank, G. P., Dusek, U., Andreae, M. O., and Poschl, U.:  
953 Calibration and measurement uncertainties of a continuous-flow cloud condensation nuclei counter  
954 (DMT-CCNC): CCN activation of ammonium sulfate and sodium chloride aerosol particles in theory  
955 and experiment, *Atmos. Chem. Phys.*, 8, 1153-1179, 10.5194/acp-8-1153-2008, 2008.  
956  
957 Scanning Mobility Particle Sizer Series 5.400 and 5.500, Grimm Aerosol Technik, Ainring, Germany,  
958 2009.  
959  
960 Schmale, J., Henning, S., Decesari, S., Henzing, B., Keskinen, H., Sellegri, K., Ovadnevaite, J., Pohlker,  
961 M. L., Brito, J., Bougiatioti, A., Kristensson, A., Kalivitis, N., Stavroulas, I., Carbone, S., Jefferson, A.,  
962 Park, M., Schlag, P., Iwamoto, Y., Aalto, P., Aijala, M., Bukowiecki, N., Ehn, M., Frank, G., Frohlich,  
963 R., Frumau, A., Herrmann, E., Herrmann, H., Holzinger, R., Kos, G., Kulmala, M., Mihalopoulos, N.,  
964 Nenes, A., O'Dowd, C., Petaja, T., Picard, D., Pohlker, C., Poschl, U., Poulain, L., Prevot, A. S. H.,  
965 Swietlicki, E., Andreae, M. O., Artaxo, P., Wiedensohler, A., Ogren, J., Matsuki, A., Yum, S. S.,  
966 Stratmann, F., Baltensperger, U., and Gysel, M.: Long-term cloud condensation nuclei number  
967 concentration, particle number size distribution and chemical composition measurements at regionally  
968 representative observatories, *Atmos. Chem. Phys.*, 18, 2853-2881, 10.5194/acp-18-2853-2018, 2018.  
969  
970 Sem, G. J.: Design and performance characteristics of three continuous-flow condensation particle  
971 counters: a summary, *Atmos. Res.*, 62, 267-294, 10.1016/s0169-8095(02)00014-5, 2002.  
972  
973 Seol, K. S., Tsutani, Y., Camata, R. P., Yabumoto, J., Isomura, S., Okada, Y., Okuyama, K., and  
974 Takeuchi, K.: A differential mobility analyzer and a Faraday cup electrometer for operation at 200-930  
975 Pa pressure, *J. Aerosol. Sci.*, 31, 1389-1395, 10.1016/s0021-8502(00)00037-9, 2000.

976  
977 Sinnarwalla, A. M. a. A., D.J.: A Cloud Nucleus Counter with Long Available Growth Time, Journal of  
978 Applied Meteorology, 831-835, 1973.  
979  
980 Stratmann, F., Kauffeldt, T., Hummes, D., and Fissan, H.: Differential electrical mobility analysis: A  
981 theoretical study, Aerosol Sci. Technol., 26, 368-383, 10.1080/02786829708965437, 1997.  
982  
983 Sullivan, R. C., Moore, M. J. K., Petters, M. D., Kreidenweis, S. M., Roberts, G. C., and Prather, K. A.:  
984 Timescale for hygroscopic conversion of calcite mineral particles through heterogeneous reaction with  
985 nitric acid, Phys. Chem. Chem. Phys., 11, 7826-7837, 10.1039/b904217b, 2009.  
986  
987 Svenningsson, B., Rissler, J., Swietlicki, E., Mircea, M., Bilde, M., Facchini, M. C., Decesari, S., Fuzzi,  
988 S., Zhou, J., Monster, J., and Rosenorn, T.: Hygroscopic growth and critical supersaturations for mixed  
989 aerosol particles of inorganic and organic compounds of atmospheric relevance, Atmos. Chem. Phys., 6,  
990 1937-1952, 10.5194/acp-6-1937-2006, 2006.  
991  
992 Wiedensohler, A.: An approximation of the bipolar charge distribution for particles in the sub-micron  
993 size range, J. Aerosol. Sci., 19, 387-389, 10.1016/0021-8502(88)90278-9, 1988.  
994  
995 Winkler, P.: The growth of atmospheric aerosol particles as a function of the relative humidity. II. An  
996 improved concept of mixed nuclei, J. Aerosol. Sci., 4, 373-387, 1973.  
997  
998 Zhao-Ze, D., and Liang, R.: Highly biased hygroscopicity derived from size-resolved cloud  
999 condensation nuclei activation ratios without data inversion, Atmospheric and Oceanic Science Letters,  
1000 7, 254-259, 2014.  
1001  
1002



Notation	
$\alpha_{cc}, \beta_{cc}, \gamma_{cc}$	Empirically-determined constants used to calculate Cunningham slip correction factor
$Z_p$	Aerosol particle electrical mobility
$C_c$	Cunningham slip correction factor
$d_m$	Electrical mobility diameter
$n$	Number of charges on particle
$e$	Elementary unit of charge
$\eta$	Gas dynamic viscosity
$\lambda$	Mean free path
$Q_{sh}$	Sheath flow
$Q_e$	Excess air flow
$Q_a$	Aerosol flow
$Q_s$	Sample flow
$\kappa_{app}$	Apparent hygroscopicity parameter
$\kappa_{app,artifact}$	Apparent hygroscopicity parameter artifact
$s$	Equilibrium water vapor saturation
$s_{crit}$	Critical saturation (50 % of aerosols active as cloud condensation nuclei)
$A$	Constant used in calculating $\kappa_{app}$
$\sigma_{lv}$	Surface tension of water
$T$	Temperature
$D_{act}$	Activation diameter
$SS_{crit}$	Critical percent supersaturation
$\alpha_{TF}$	Height of DMA transfer function
$\beta_{TF}$	Half-width of DMA transfer function
$Z'_p$	Mobility of particle at DMA inlet
$Z_{p,mid}$	Midpoint of transfer function
$\Delta Z_p$	Half-width of transfer function
$V_0$	Voltage selected at DMA
$r_1$	DMA inner radius
$r_2$	DMA outer radius
$L$	DMA length
$d_{50}$	50 %-cut-off diameter

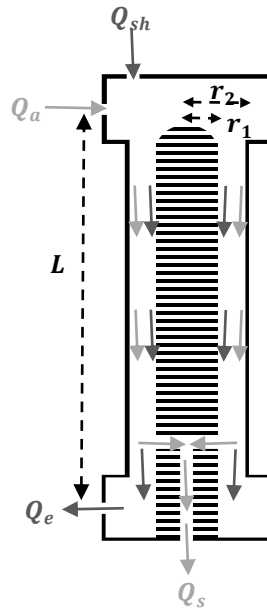
1003



1004

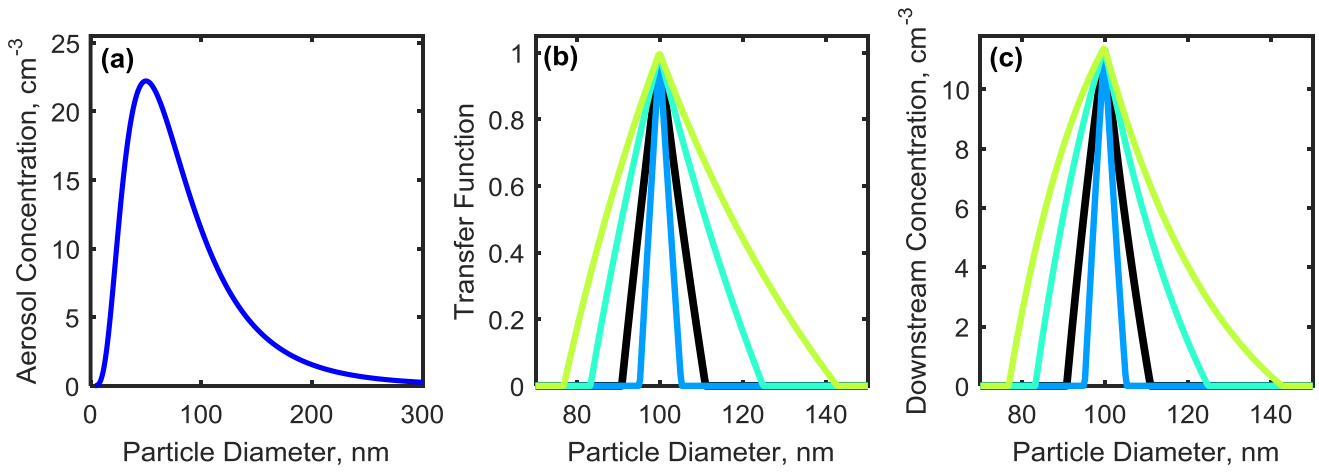
1005 **Figure 1** Experimental setup used for obtaining sized CCN and particle concentration measurements

1006 from an aerosol sample.



1007

1008 **Figure 2** Simplified flow diagram of a DMA with an inner electrode radius  $r_1$ , outer electrode radius  $r_2$ ,  
 1009 distance between aerosol inlet and sample outlet  $L$ , clean sheath air flow  $Q_{sh}$ , aerosol flow  $Q_a$ , excess air  
 1010 flow  $Q_e$ , and sample air flow  $Q_s$ .



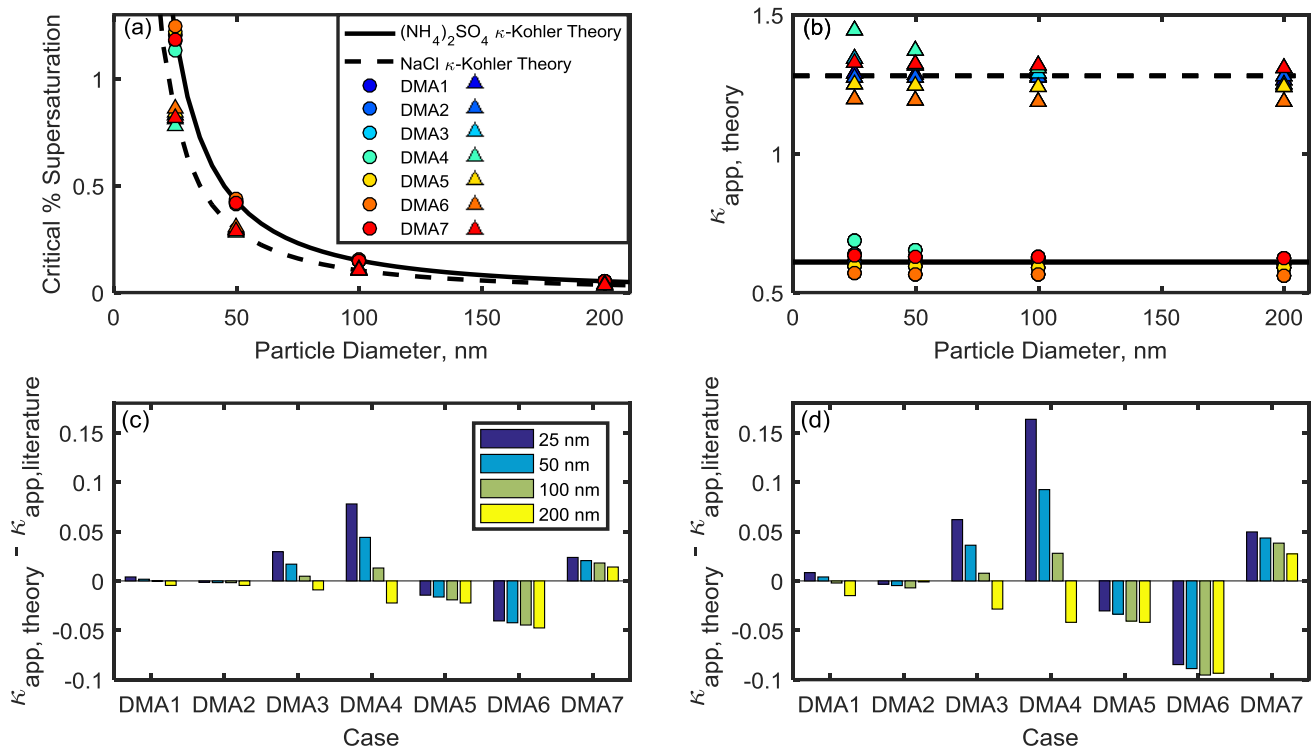
1011

1012

1013 **Figure 3** (a) A theoretical aerosol distribution generated using a lognormal function centered at 50 nm. .

1014 (b) The transfer function calculated using Eq. (7). (c) Multiplying the distribution by the transfer function

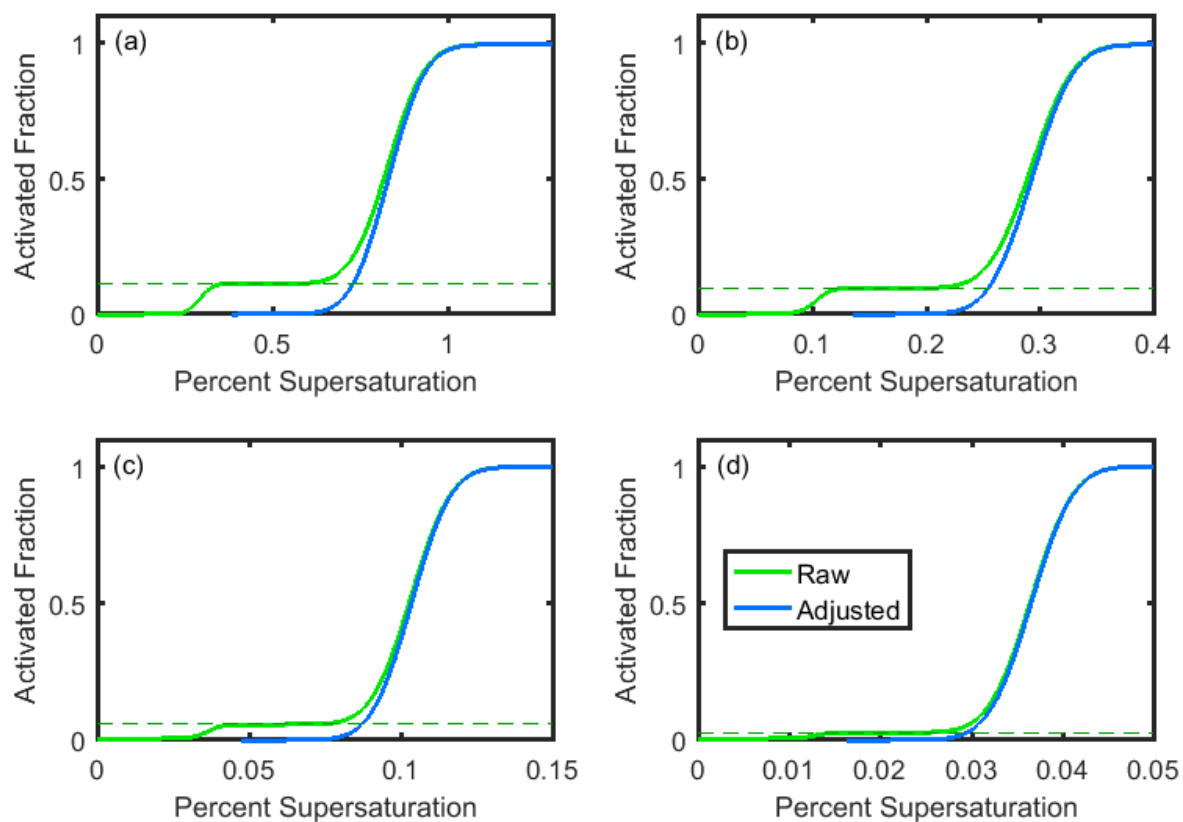
1015 gives the downstream aerosol concentration ( $\text{cm}^{-3}$ ).



1016

1017

1018 **Figure 4** (a) Critical supersaturation of ammonium sulfate and sodium chloride particles calculated for DMA  
 1019 Cases 1-7 for sodium chloride (triangles) and ammonium sulfate (circles). Ammonium sulfate and sodium  
 1020 chloride curves from  $\kappa$ -Köhler theory are shown for comparison. (b) Apparent hygroscopicity  $\kappa_{app}$  for  
 1021 DMA cases 1-7. (c) DMA-flow-derived artifacts in ammonium sulfate  $\kappa_{app}$  are shown for each DMA case.  
 1022 (d) DMA-flow-derived artifacts in sodium chloride  $\kappa_{app}$  are shown for each DMA case.



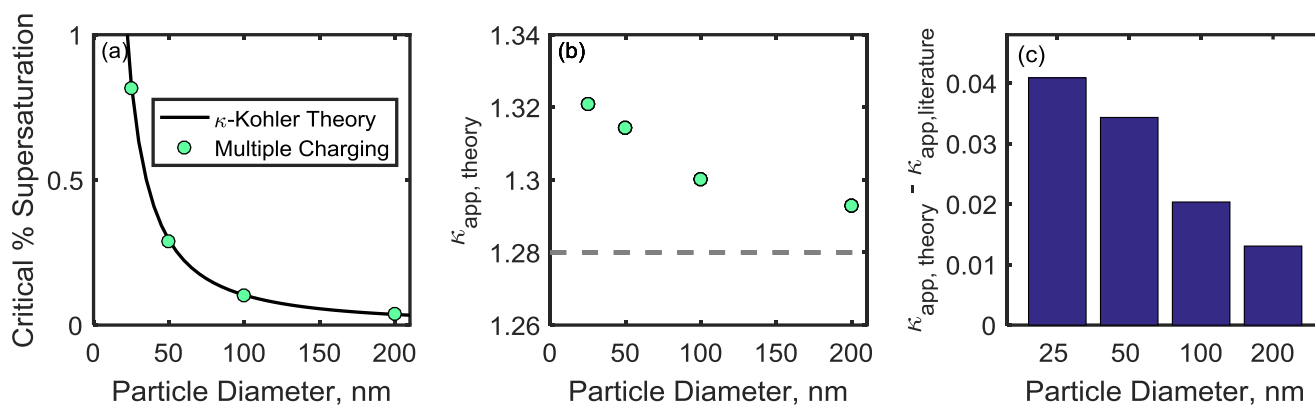
1023

1024 **Figure 5** Theoretical raw (green) and adjusted (blue) activated fraction curves for (a) 25 nm (+1), 50 nm

1025 (+2), and 75 nm (+3) particles; (b) 50 nm (+1), 100 nm (+2), and 150 nm (+3) particles; (c) 100 nm

1026 (+1), 200 nm (+2), and 300 nm (+3) particles; (d) 200 nm (+1), 400 nm (+2), and 600 nm (+3) particles.

1027 All particles are pure sodium chloride.

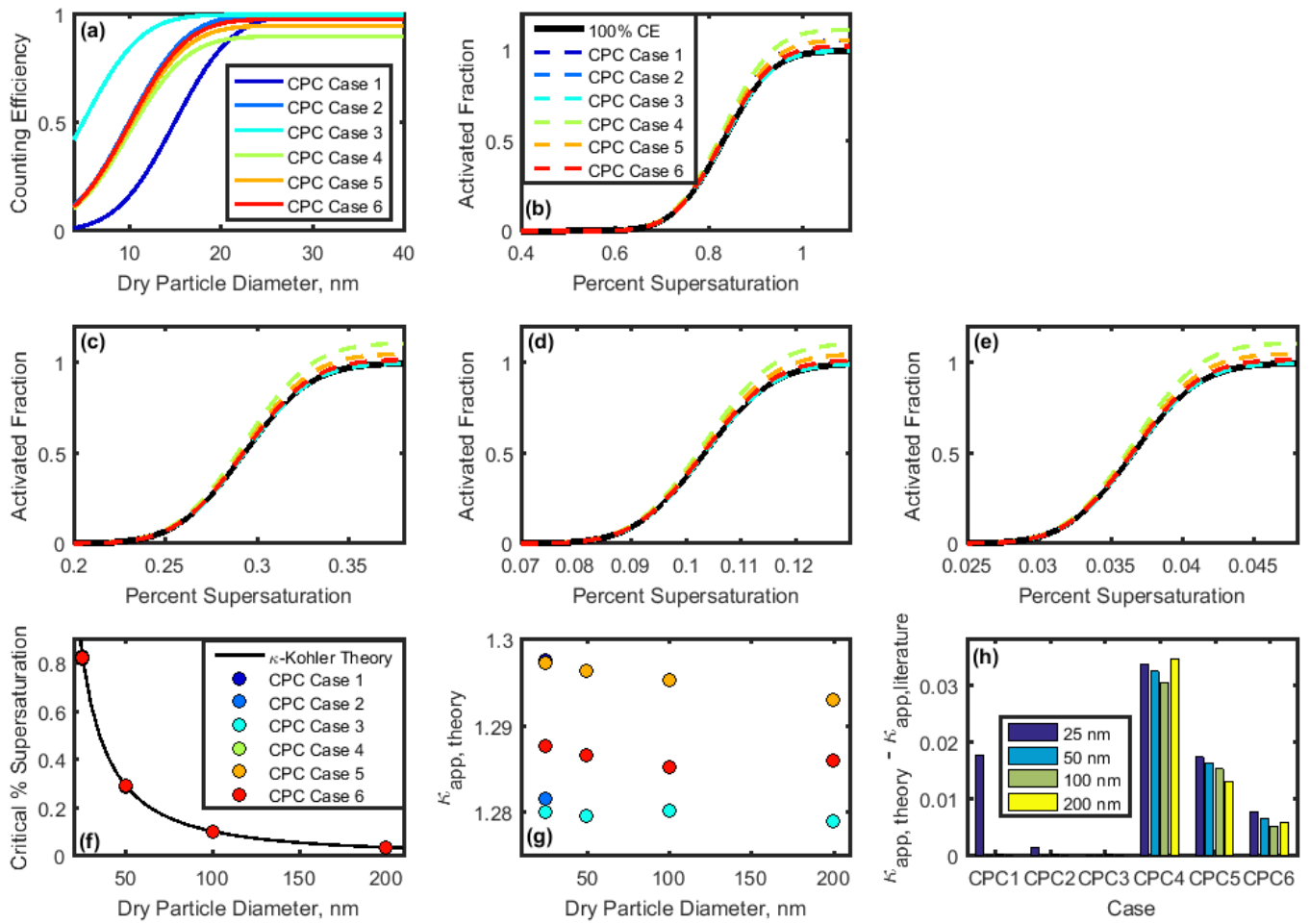


1028

1029 **Figure 6** (a) Critical percent supersaturation of sodium chloride particles determined from activated  
 1030 fraction curves shown in Fig. 5. A  $\kappa$ -Köhler curve for sodium chloride is shown for comparison. (b)

1031 Theoretical  $\kappa_{app}$  for each particle diameter (gray dashed line indicates literature value for  $\kappa_{app}^{NaCl}$ ). (c)

1032 Artifacts in  $\kappa_{app}$  resulting from multiple particle charges.



1033

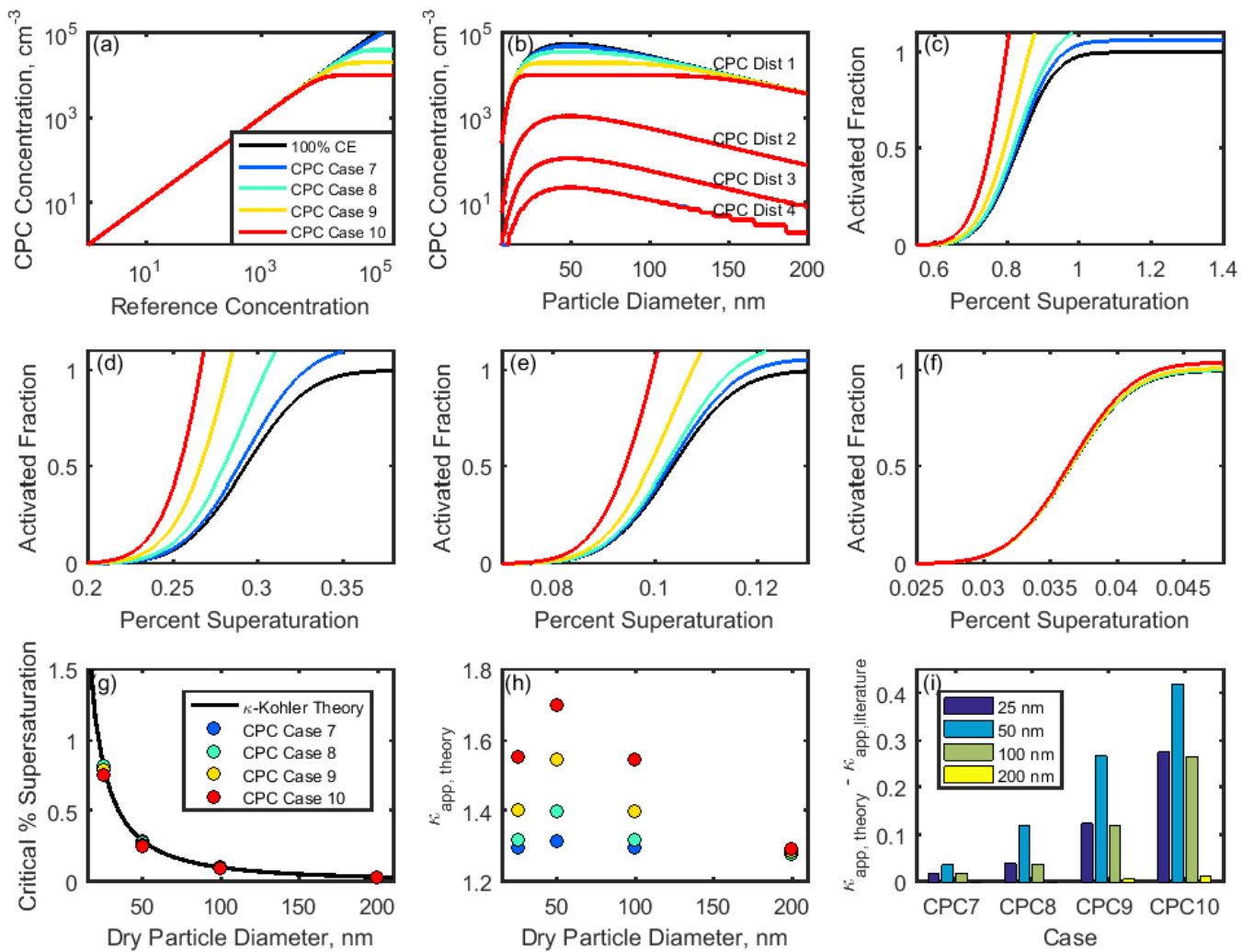
1034 **Figure 7** (a) Counting efficiency curves for CPC Cases 1-6 (shown in Table 3).

1035 (b-e) CCN activated fraction curves for 25, 50, 100, and 200 nm NaCl, respectively. (f) Critical

1036 supersaturation calculated for each particle diameter. (g) Theoretical  $\kappa_{app}$  for each CPC case and

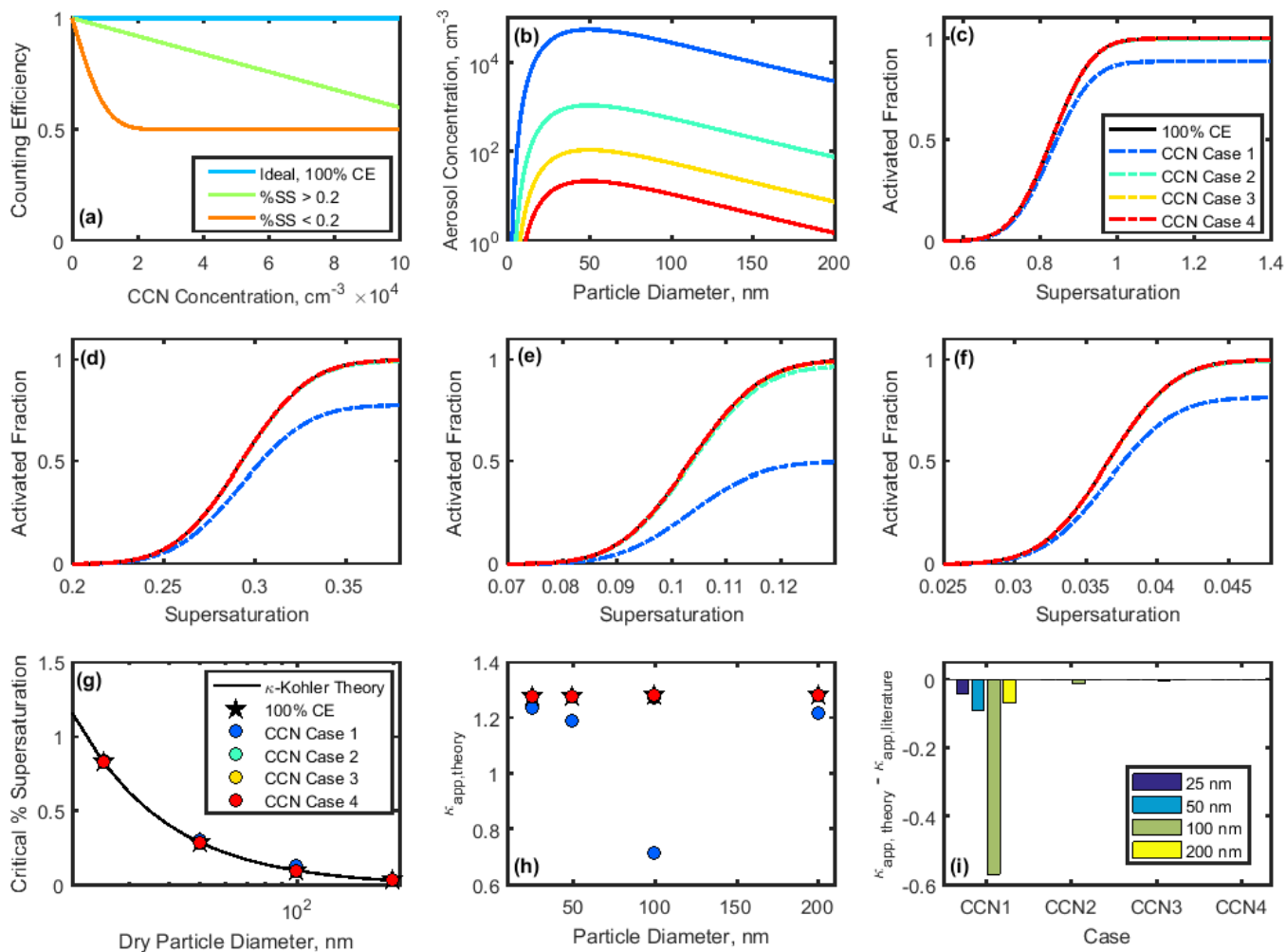
1037 particle diameter. (h) Artifacts in  $\kappa_{app}$  for each CPC case and particle diameter.





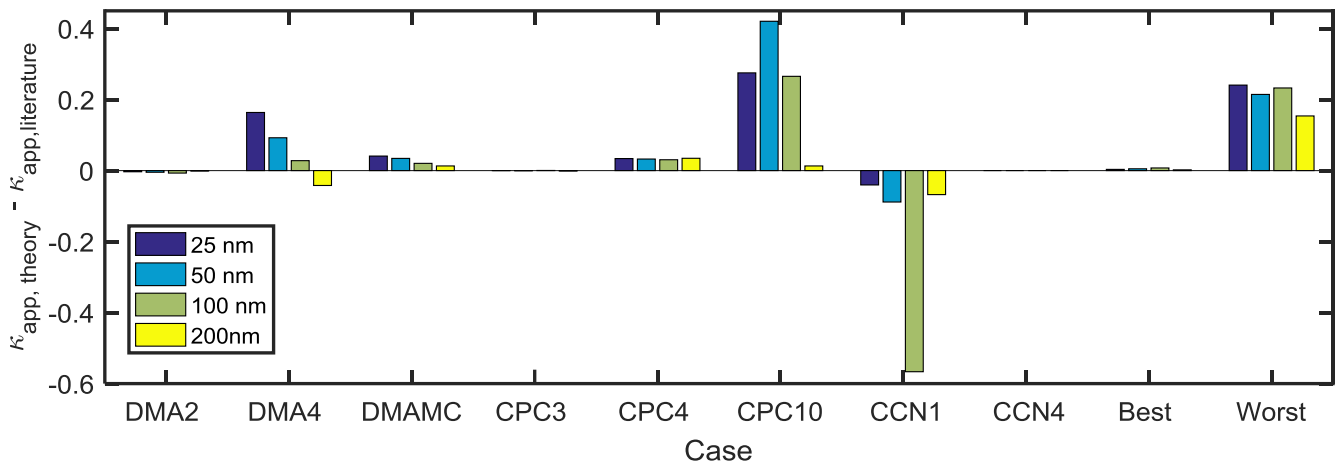
1038

1039 **Figure 8** (a) Theoretical relationships between the reference aerosol concentration and CPC  
 1040 concentration. (b) Concentration-dependent counting efficiencies from (a) were applied to four  
 1041 theoretical aerosol distributions. (c-f) Activated fraction curves for CPC Distribution 1 and particle  
 1042 diameters 25, 50, 100, and 200 nm NaCl aerosol, respectively. (g,h) Critical supersaturation and  $\kappa_{app}$  for  
 1043 each case. (i) Artifacts in  $\kappa_{app}$  for each case.



1044

1045 **Figure 9** (a) Counting efficiencies of the DMT CCN-100 for specific supersaturations. (b) Lognormal  
 1046 aerosol distributions used to study CCN undercounting at high concentrations. (c-f) Activated fraction  
 1047 curves for 25, 50, 100, and 200 nm NaCl particles. Supersaturation-specific counting efficiencies from  
 1048 (a) applied to theoretical sigmoid curves for NaCl CCN activation. Activated fraction in the case of 100  
 1049 % counting efficiency is shown for comparison. (g) Critical supersaturation for each case. (h)  
 1050 Theoretical  $\kappa_{app}$  calculated for each case. (i) Artifacts in  $\kappa_{app}$  artifacts for each case.



1051

1052 **Figure 10** Comparison of  $\kappa_{app}$  artifacts derived from best and worst case scenarios for instrumental  
 1053 measurements for sodium chloride. Combined artifacts for the lowest-artifact cases (Best: DMA Case  
 1054 2, CPC Case 3, and CCN Case 4) and the highest-artifact cases (Worst: DMA Case 4, multiple charging,  
 1055 CPC Case 4, CPC Case 8, and CCN Case 1).

1056

**Table 1 Theoretical DMA Flow Test Cases**

<b>Case</b>	$Q_{sh}$ (L min <sup>-1</sup> )	$Q_e$ (L min <sup>-1</sup> )	$Q_a$ (L min <sup>-1</sup> )	$Q_s$ (L min <sup>-1</sup> )	$Q_a/Q_{sh}$	$Q_e/Q_{sh}$
<b>DMA 1</b>	3.00	3.00	0.30	0.30	0.10	1.00
<b>DMA 2</b>	3.00	3.00	0.15	0.15	0.05	1.00
<b>DMA 3</b>	3.00	3.00	0.60	0.60	0.20	1.00
<b>DMA 4</b>	3.00	3.00	0.90	0.90	0.30	1.00
<b>DMA 5</b>	3.00	3.06	0.36	0.30	0.12	1.02
<b>DMA 6</b>	3.00	3.15	0.45	0.30	0.15	1.05
<b>DMA 7</b>	3.00	2.94	0.24	0.30	0.08	0.98

1057

**Table 2 Predicted downstream particle diameter range for each DMA case.**

<b>Case</b>	<b>25 nm</b>	<b>50 nm</b>	<b>100 nm</b>	<b>200 nm</b>
<b>DMA 1</b>	23-27	46-56	91-111	181-222
<b>DMA 2</b>	24-26	48-53	95-105	190-211
<b>DMA 3</b>	21-31	42-62	83-125	167-250
<b>DMA 4</b>	20-36	39-71	77-143	154-285
<b>DMA 5</b>	23-27	45-55	90-110	181-220
<b>DMA 6</b>	22-27	45-54	89-107	178-215
<b>DMA 7</b>	23-28	46-56	92-112	183-225

1058

**Table 3 Values of 50%-cutoff diameter and maximum counting efficiency used in investigating  $\kappa_{app}$  artifacts for low particle concentrations measured by a CPC.**

<b>Case</b>	<b><math>d_{50}</math>, nm</b>	<b>Maximum Counting Efficiency</b>
CPC 1	15	100 %
CPC 2	10	100 %
CPC 3	5	100 %
CPC 4	10	90 %
CPC 5	10	95 %
CPC 6	10	98 %

1059

**Table 4** Equations used to model the relationship between a reference or “true” aerosol concentration  $x$  (particles  $\text{cm}^{-3}$ ), and the concentration measured by a condensation particle counter  $y$  (particles  $\text{cm}^{-3}$ ).

Case	Equation
CPC 7	$y = x - 2 \times 10^{-6}x^2$
CPC 8	$y = 40000 \operatorname{erf}\left(\frac{x}{32000\sqrt{2}}\right)$
CPC 9	$y = 20000 \operatorname{erf}\left(\frac{x}{16000\sqrt{2}}\right)$
CPC 10	$y = 10000 \operatorname{erf}\left(\frac{x}{8000\sqrt{2}}\right)$

1060

**Table 5 Total concentrations used in theoretical aerosol distribution for CPC operation at high concentration and CCN-derived  $\kappa_{app}$  artifacts.**

<b>CPC Distribution</b>	<b>CCN Case</b>	<b>Total Concentration (particles cm<sup>-3</sup>)</b>
CPC Distribution 1	CCN 1	$5 \times 10^6$
CPC Distribution 2	CCN 2	$1 \times 10^5$
CPC Distribution 3	CCN 3	$1 \times 10^4$
CPC Distribution 4	CCN 4	$2 \times 10^3$

1061